Post-capture attitude control with prescribed performance

Xiuwei Huang[a,*], James D. Biggs[b], Guangren Duan[a,c]

[a] *Center for Control Theory and Guidance Technology, Harbin Institute of Technology, Harbin 150001, P. R. China*
[b] *Department of Aerospace Science and Technology, Polytechnic University of Milan, Milano 20156, Italy*
[c] *State Key Laboratory of Robotics and System, Harbin Institute of Technology, Harbin 150001, P. R. China*

Abstract

The capture or docking of a spacecraft with a target spacecraft is an important component of future space debris capture and orbit servicing missions. One proposed concept includes using a robotic arm mounted on the chaser spacecraft to connect and manipulate the target's motion. This paper focuses on the post-capture attitude control of the target which will bring the target to rest and then control it in a prescribed way. The attitude control can be achieved by designing a robust control in the known chaser reference frame and treating the dynamics due to the uncertain inertia as an unknown disturbance. However, this can lead to poor performance since this uncertain torque can be large. In this paper, it is shown that the in-situ construction of the chaser-target dynamics can lead to improved performance. Based on the combined re-constructed model, a new disturbance observer based control with robust dynamic control allocation is developed. This approach is robust to the uncertainties in the re-constructed model and enables the prescription of convergence and stability properties. The proposed approach is demonstrated through numerical simulation of an actively controlled 12U CubeSat that has captured an inactive 12U CubeSat spacecraft.

Keywords: attitude control, dynamic surface control, nonlinear disturbance observer, robust dynamic control allocation, actuator saturation, combined spacecraft

1. Introduction

New space mission scenarios include the requirement of a chaser spacecraft to dock [1, 2], service or capture a target spacecraft [3, 4]. One possibility for service and capture is to use a robotic arm to grasp the moving target [5, 6]. The next phase is then to de-tumble the connected chaser-target and re-orient the

*Corresponding author
Email addresses: huangxiuwei_hit@163.com (Xiuwei Huang), jamesdouglas.biggs@polimi.it (James D. Biggs), g.r.duan@hit.edu.cn (Guangren Duan)

combined system in a prescribed direction. One approach [7, 8] for the attitude control of the combined system is to model it with respect to the original body frame of the chaser, while treating the connected target as a disturbance torque. However, since the target spacecraft could be of comparable size to the chaser, this will lead to a significant disturbance that ultimately reduces the control performance when using robust control [9]. In addition, the combined chaser-target system may experience large external disturbance torques since the original thrusters used for orbital control, which originally were aligned with the centre-of-mass of the chaser spacecraft, will now be off-set from the new centre-of-mass [10]. In this paper, the dynamics and thruster configuration matrix are determined with respect to a new reference frame defined at the new centre-of-mass of the combined system. This enables the control to be defined based on the true dynamics of the spacecraft and actuator configuration. This new model can then be used to design a robust control and dynamic control allocation method with significantly improved performance.

The development of a new model of the combined chaser-target has been addressed in [11], but in this case the direction vectors of the thrusters were assumed to be known in the new body frame. In this paper, the configuration matrix of the thrusters is determined in the new body-frame of the chaser-target system using only knowledge of the centre of mass. However, even with an improved in-situ model there will still exist an estimation error in the position vectors of the thrusters in the new body frame. To address this problem, a robust control allocation is presented that maps an 'ideal' virtual control to each thruster. In [12] and [13], a robust control allocation (RobCA) strategy, formulated as a min-max optimization problem, was proposed to redistribute a virtual control signal to the remaining actuators when an actuator fault occurred. However, dynamic properties during the control allocation process were not considered. Dynamic control allocation depends on the distribution in both current and previous sampling instants [14], which could allow different actuators to produce control efforts at different frequency ranges. In [15], a constrained quadratic programming-based robust dynamic control allocation was implemented to manage the use of the redundant actuators. A dynamic control allocation algorithm that incorporates both actuator saturation and rate constraints was proposed in [16] and [17]. In this paper, a robust dynamic control allocation (RobDCA) method that considers both the amplitude and rate constraints of the low-thrust propulsion is proposed which also accounts for thrust vector uncertainty.

The 'virtual' control that is the input to the RobDCA is designed such that prescribed performances in terms of convergence time, stability and accuracy can be prescribed a priori. The ability to prescribe performance a priori even in the presence of disturbances is of significant practical importance since it negates the need for extensive monte-carlo numerical testing. The first prescribed performance controls

were developed in the mathematical control literature by Bechlioulis [18], [19] where the control scheme guarantees a prescribed performance for a class of feedback linearizable nonlinear systems. Moreover, for this class of system the control designer can prescribe an arbitrarily small residual set for the tracking error; a convergence rate no less than a prescribed value and a prescribed maximum overshoot. A number of prescribed performance controls using different techniques have been proposed such as sliding mode control [20], adaptive feedback control [21, 22, 23], disturbance-observer based control [24] and neural network based control [25, 26, 27]. Also, the influence of the control constraint on the system performance needs to be considered in the control design. Such practical constraints can be dealt with using a command governor [28] or anti-windup compensator [29]. In addition, the backstepping control [30] is one of the most popular design tools for a systematic nonlinear control synthesis, and has been successfully applied to prescribed-performance attitude control. However, the main drawback of backstepping is that the resulting control law becomes highly non-linear and complex since the relative degree of the system is high due to the need to repeatedly differentiate nonlinear functions, a problem that has been called an 'explosion of complexity' [31]. In this paper, a disturbance-observer-based dynamic surface control method is used to develop the virtual attitude control. This approach enables the control engineer to prescribe closed-loop performances in the presence of input saturation, inertia uncertainties and external disturbances. Significantly it is shown that this control can deal with the parasitic torque induced by the shift in the centre of mass of the system post-capture.

The main contribution of this paper is a prescribed-performance attitude control for a combined chaser-target system, with significant internal and external uncertainties, where the chaser spacecraft is actuated using low-thrust propulsion. The key components of the presented prescribed attitude control synthesis are:

1. The development of an approach to define the attitude dynamics with orbit control torque of the combined chaser-target system, by using the knowledge of the position of the new center-of-mass which is estimated in-situ. This is in contrast to [11] which requires the direction vectors of the thrusters to be known and does not consider the orbit control torque.

2. A nonlinear disturbance observer in which only one parameter needs to be tuned to estimate the lumped uncertainties. This simplifies the implementation process compared to the prescribed controls in [13, 21, 25, 27].

3. A robust dynamic control allocation scheme that takes into account the uncertainties induced by post-capture of the target, where an optimal solution can be obtained by simple LMI-based programming. In contrast, only the dynamic situation of control allocation is considered in [14, 15, 16, 17].

This paper is presented as follows: In section 2, the attitude dynamics of combined spacecraft with orbit control torque is established under external disturbances, inertia uncertainties and actuator saturation. A disturbance-observer-based dynamic surface control scheme is developed to ensure that the closed-loop system response satisfies prescribed performances in section 3. In section 4, a RobDCA method is presented for saturated thrusters. Finally, numerical simulations provided in Section 5 illustrate the performance of the control law and RobDCA, and the necessity to use a new combined dynamics and thruster configuration model.

2. Attitude kinematics and dynamics of a combined chaser-target system

The combined spacecraft system consists of a rigid chaser spacecraft and a rigid, uncontrolled, target spacecraft connected with a rigid manipulator. Once the target has been captured, the combined chaser-target system can be considered as a rigid body [32, 33] as shown in Figure 1 with the following assumptions: (1) The chaser spacecraft is driven by a continuous low-thrust propulsion. (2) The space manipulators of the chaser are locked rigidly to the target spacecraft. (3) The target spacecraft is inactive and captured by the chaser. (4) The effect of plume impact is neglected. (5) The position of the mass center of the combined spacecraft is known. This assumption is based on the post-capture centre-of-mass estimation technique proposed using in-situ least squares estimation [34].

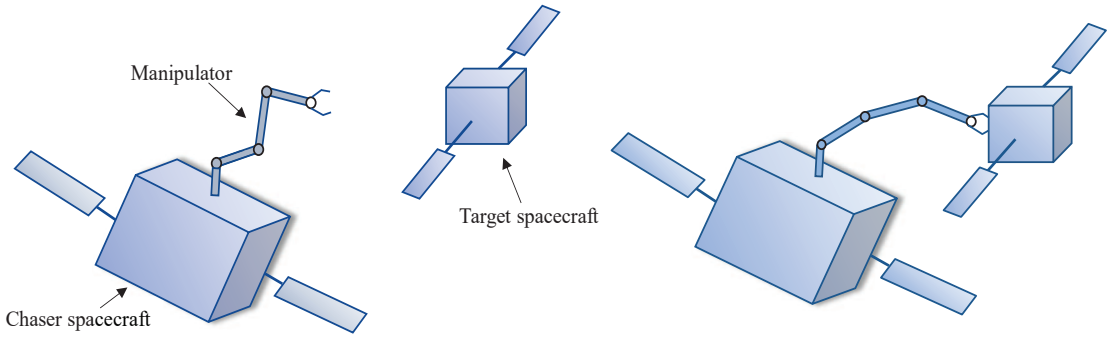

Figure 1: Before and after capture of target using space robot

To simplify the description, we define the body frame of the chaser spacecraft as $\sum O_s$ which is located at the centre-of-mass of chaser spacecraft O_s, the body frame of the combined spacecraft is defined as $\sum O_c$ which is located at the centre-of-mass of the combined spacecraft O_c. Also, we define the attitude rotation matrix from frame $\sum O_s$ to $\sum O_c$ as $\boldsymbol{R}_{sc}$ and define the position vector from O_s to O_c as $\boldsymbol{r}_c$ expressed in the

frame $\sum O_s$.

In this paper, the Modified Rodrigues Parameters (MRPs) vector $\boldsymbol{\sigma} = \mathbf{e}\tan(\vartheta/4) = [\sigma_1, \sigma_2, \sigma_3]^{\mathrm{T}} \in \mathbb{R}^3$ with Euler's principal rotation axis $\mathbf{e}$ and angle ϑ is used to represent the combined spacecraft's attitude orientation in the frame $\sum O_c$. The kinematic model of combined spacecraft in terms of the MRPs can be expressed as

$$\dot{\boldsymbol{\sigma}} = \boldsymbol{G}(\boldsymbol{\sigma})\boldsymbol{\omega} \tag{1}$$

where $\boldsymbol{G}(\boldsymbol{\sigma}) = \frac{1}{4}[(1 - \boldsymbol{\sigma}^{\mathrm{T}}\boldsymbol{\sigma})\boldsymbol{I}_3 + 2\boldsymbol{\sigma}^{\times} + 2\boldsymbol{\sigma}\boldsymbol{\sigma}^{\mathrm{T}}]$, $\boldsymbol{\omega} \in \mathbb{R}^3$ is the angular velocity of the combined spacecraft expressed in the frame $\sum O_c$. Here, $\boldsymbol{\sigma}^{\times} \in \mathbb{R}^{3\times3}$ is the skew-symmetric operator that carries a 3×1 vector into a 3×3 matrix

$$\boldsymbol{\sigma}^{\times} = \begin{bmatrix} 0 & -\sigma_3 & \sigma_2 \\ \sigma_3 & 0 & -\sigma_1 \\ -\sigma_2 & \sigma_1 & 0 \end{bmatrix}$$

and satisfies $\boldsymbol{\sigma}^{\times}\boldsymbol{b} = \boldsymbol{\sigma} \times \boldsymbol{b}$ for any $\boldsymbol{b} \in \mathbb{R}^3$. If $\vartheta \to 360$ deg, the corresponding MRPs will go singular. It is possible to map the MRPs vector $\boldsymbol{\sigma}$ to its shadow counterpart $\boldsymbol{\sigma}^s$ through $\boldsymbol{\sigma}^s = \frac{\boldsymbol{\sigma}}{\boldsymbol{\sigma}^{\mathrm{T}}\boldsymbol{\sigma}}$ by switching the MRPs to $\boldsymbol{\sigma}^s$ when $\boldsymbol{\sigma}^{\mathrm{T}}\boldsymbol{\sigma} > 1$. In this way, the MRPs vector remains bounded within a unit sphere, and a global representation is ensured [35].

The configuration of the orbit control force is shown in Figure 2. We assume that the orbit control force is a constant vector focusing on the body point T_s whose position vector is $\boldsymbol{d}_{s0}$ expressed in the frame $\sum O_s$. Then the orbit control torque generated by the orbit-controlled engine is defined as $\boldsymbol{u}_{st}$ expressed in the frame $\sum O_s$ and

$$\boldsymbol{u}_{st} = f_0\boldsymbol{A}_{st} \tag{2}$$

where f_0 is the magnitude of orbit control force and

$$\boldsymbol{A}_{st} = \boldsymbol{d}_{s0} \times \boldsymbol{e}_{s0} \tag{3}$$

with the unit orientation vector of the orbit control force $\boldsymbol{e}_{s0}$. For the $\boldsymbol{d}_{s0}$ and $\boldsymbol{e}_{s0}$ are in the same direction, we can get that $\boldsymbol{u}_{st} = [0, 0, 0]^{\mathrm{T}}$.

From Figure 2 and using the attitude matrix $\boldsymbol{R}_{sc}$, we can find that the position vector of $\boldsymbol{T}_s$ expressed in the frame $\sum O_c$ can be denoted as

$$\boldsymbol{d}_0 = \boldsymbol{R}_{sc}(\boldsymbol{d}_{s0} - \boldsymbol{r}_c) \tag{4}$$

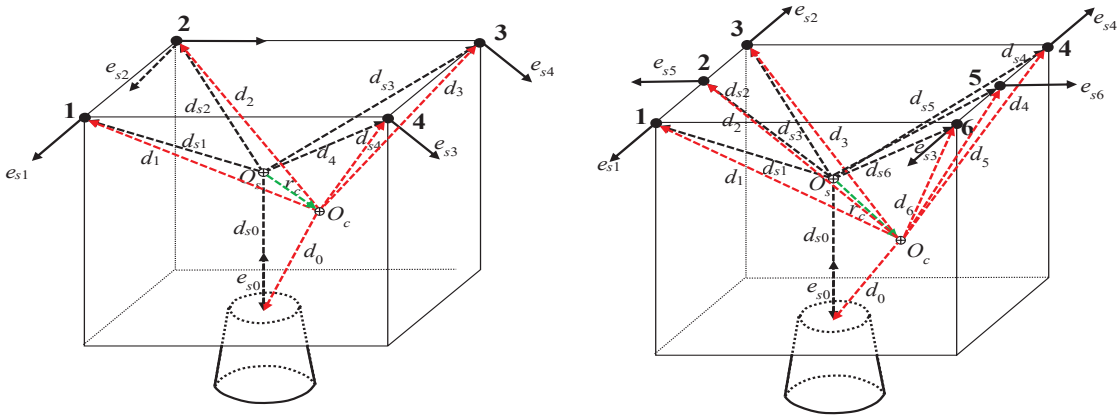

(a) Four thrusters with orbit control torque

(b) Six thrusters with orbit control torque

Figure 2: Thruster configuration with orbit control torque

where the $\boldsymbol{r}_c$ is the vector from position O_s to O_c expressed in frame $\sum O_s$ and $\boldsymbol{e}_{s0}$ expressed in the frame $\sum O_c$ can be denoted as

$$\boldsymbol{e}_0 = \boldsymbol{R}_{sc}\boldsymbol{e}_{s0} \tag{5}$$

Then the control toque generated by the orbit-controlled engine expressed in the frame $\sum O_c$ is

$$\boldsymbol{u}_t = f_0\boldsymbol{A}_t \tag{6}$$

where

$$\boldsymbol{A}_t = \boldsymbol{d}_0 \times \boldsymbol{e}_0 \tag{7}$$

In this paper, we consider that there are N thrusters in the attitude control system, with $N \geq 4$ required for controllability [36]. Figure 2 shows two particular cases of thruster configuration, i.e. four and six thrusters with orbit control torque. We assume that the position vector of the i-th thruster expressed in the frame $\sum O_s$ is defined as $\boldsymbol{d}_s$, $i = 1, 2, \cdots, N$. We also define the unit orientation vector and control force magnitude of the i-th thruster are $\boldsymbol{e}_{si}$ and f_i $(i = 1, 2, \cdots, N)$ expressed in the frame $\sum O_s$, respectively. From Figure 2 and using the attitude rational matrix $\boldsymbol{R}_{sc}$, we can find that the position vector of thrusters expressed in the frame $\sum O_c$ can be denoted as

$$\boldsymbol{d}_i = \boldsymbol{R}_{sc}(\boldsymbol{d}_{si} - \boldsymbol{r}_c),\ i = 1, 2, \cdots, N \tag{8}$$

and the unit orientation vector of the i-th thruster expressed in the frame $\sum O_c$ is

$$\boldsymbol{e}_i = \boldsymbol{R}_{sc}\boldsymbol{e}_{si},\ i = 1, 2, \cdots, N \tag{9}$$

Defining the control torque generated by the thrusters expressed in the frame $\sum O_c$ as $\boldsymbol{u}_c$, we have

$$\boldsymbol{u}_c = \boldsymbol{A}_c \boldsymbol{F} \tag{10}$$

with

$$\boldsymbol{A}_c = [\boldsymbol{a}_1, \boldsymbol{a}_2, \cdots, \boldsymbol{a}_N] \tag{11}$$

$$\boldsymbol{F} = [f_1, f_2, \cdots, f_N]^{\mathrm{T}} \tag{12}$$

and

$$\boldsymbol{a}_i = \boldsymbol{d}_i \times \boldsymbol{e}_i,\ i = 1, 2, \cdots, N \tag{13}$$

Thus the dynamics of the combined chaser-target system with orbit control torque can be described as:

$$\boldsymbol{J}\dot{\boldsymbol{\omega}} + \boldsymbol{\omega}^{\times}\boldsymbol{J}\boldsymbol{\omega} = \boldsymbol{u}_c + \boldsymbol{u}_t + \boldsymbol{u}_g + \boldsymbol{d} \tag{14}$$

where $\boldsymbol{J} \in \mathbb{R}^{3\times3}$ is the inertial matrix of combined spacecraft expressed in $\sum O_c$, $\boldsymbol{d} \in \mathbb{R}^3$ is the bounded external disturbance.

Remark 1. *External disturbance torques in Low Earth Orbit are due to solar radiation, gravity gradient torque, the interaction of the Earth's magnetic field with the spacecraft's on-board electronics, and aerodynamic drag. The magnitude of these external disturbances are within the orders of* 10^{-6} *Nm and* 10^{-4} *Nm. This difference in magnitude depends critically on the offset of the centre-of-mass of the spacecraft from its geometric centre and on the sizing and positioning of the solar panels. In this paper, a disturbance of magnitude* 1×10^{-4} *Nm is chosen to account for the "worst case" environmental disturbance torques.*

And $\boldsymbol{u}_g$ is the gravity gradient torque computed by [11]

$$\boldsymbol{u}_g = 3\omega_0^2 \boldsymbol{R}_3^{\times}(\boldsymbol{\sigma})\boldsymbol{J}\boldsymbol{R}_3(\boldsymbol{\sigma}) \tag{15}$$

where ω_0 is the orbit angular rate value; $\boldsymbol{R}_3(\boldsymbol{\sigma}) \in \mathbb{R}^3$ is the third column vector of the direction cosine matrix $\boldsymbol{R}(\boldsymbol{\sigma})$ expressed as [11]

$$\boldsymbol{R}_3(\boldsymbol{\sigma}) = \frac{1}{(1+\boldsymbol{\sigma}^{\mathrm{T}}\boldsymbol{\sigma})}\begin{bmatrix} 8\sigma_1\sigma_3 - 4\sigma_2(1-\boldsymbol{\sigma}^{\mathrm{T}}\boldsymbol{\sigma}) \\ 8\sigma_2\sigma_3 + 4\sigma_1(1-\boldsymbol{\sigma}^{\mathrm{T}}\boldsymbol{\sigma}) \\ 4(\sigma_3^2 - \sigma_2^2 - \sigma_1^2) + (1-\boldsymbol{\sigma}^{\mathrm{T}}\boldsymbol{\sigma})^2 \end{bmatrix} \tag{16}$$

The inertia property of the combined chaser-target is difficult to obtain from the ground but can be estimated by on-line identification[11]. However, the estimation algorithm will naturally have errors between the true inertia matrix and estimated one of combined spacecraft which can be expressed as

$$\boldsymbol{J} = \boldsymbol{J}_0 + \Delta\boldsymbol{J} \tag{17}$$

where $\boldsymbol{J}_0$ denotes the estimated value of the inertia matrix of the combined spacecraft, $\Delta\boldsymbol{J}$ denotes the estimated error of the inertia matrix of the combined spacecraft and is bounded. The inverse matrix of $\boldsymbol{J}$ is written as

$$\boldsymbol{J}^{-1} = \boldsymbol{J}_0^{-1} + \Delta\tilde{\boldsymbol{J}} \tag{18}$$

where $\Delta\tilde{\boldsymbol{J}} = -\boldsymbol{J}_0^{-1}\Delta\boldsymbol{J}(\boldsymbol{I}_3 + \boldsymbol{J}_0^{-1}\Delta\boldsymbol{J})^{-1}\boldsymbol{J}_0^{-1}$ [37]. The kinematics and dynamics of the combined chaser-target system can be written as

$$\begin{cases} \dot{\boldsymbol{\sigma}} = \boldsymbol{G}(\boldsymbol{\sigma})\boldsymbol{\omega} \\ \dot{\boldsymbol{\omega}} = -\boldsymbol{J}_0^{-1}\boldsymbol{\omega}^{\times}\boldsymbol{J}_0\boldsymbol{\omega} + \boldsymbol{B}\boldsymbol{u}_c + \boldsymbol{B}\boldsymbol{u}_t + \boldsymbol{u}_{g0} + \boldsymbol{\delta} \end{cases} \tag{19}$$

where $\boldsymbol{B} = \boldsymbol{J}_0^{-1}$ and

$$\begin{aligned} \boldsymbol{u}_{g0} &= 3\omega_0^2\boldsymbol{J}_0^{-1}\boldsymbol{R}_3^{\times}(\boldsymbol{\sigma})\boldsymbol{J}_0\boldsymbol{R}_3(\boldsymbol{\sigma}) \\ \boldsymbol{\delta} &= -\Delta\tilde{\boldsymbol{J}}\boldsymbol{\omega}^{\times}\boldsymbol{J}\boldsymbol{\omega} - \boldsymbol{J}_0^{-1}\boldsymbol{\omega}^{\times}\Delta\boldsymbol{J}\boldsymbol{\omega} + \Delta\tilde{\boldsymbol{J}}\boldsymbol{u}_c + \Delta\tilde{\boldsymbol{J}}\boldsymbol{u}_t \\ &\quad + 3\omega_0^2\boldsymbol{J}_0^{-1}\boldsymbol{R}_3^{\times}(\boldsymbol{\sigma})\Delta\boldsymbol{J}\boldsymbol{R}_3(\boldsymbol{\sigma}) + \Delta\tilde{\boldsymbol{J}}\boldsymbol{u}_g + \boldsymbol{J}^{-1}\boldsymbol{d} \end{aligned}$$

3. Control system design

In this section, a dynamic surface 'virtual' controller with prescribed performance is proposed. This control drives the error state to zero within prescribed bounds by compensating the uncertainties induced by the target capture via a disturbance observer. Furthermore, the stability of the closed-loop system is verified based on Lyapunov stability theory and a law that assists in the tuning of the control gains is given. The structure of the proposed attitude stabilization scheme is shown in Figure 3.

3.1. Control law design

In this subsection, a disturbance-observer-based controller with prescribed performance is designed for the nonlinear system (19) with lumped disturbance containing inertia uncertainties, external disturbance and actuator saturation. By the prescribed performance control (PPC) technique, the 'constrained' attitude of system (19) is transformed into an 'unconstrained' vector. Based on the transformed vector, a dynamic

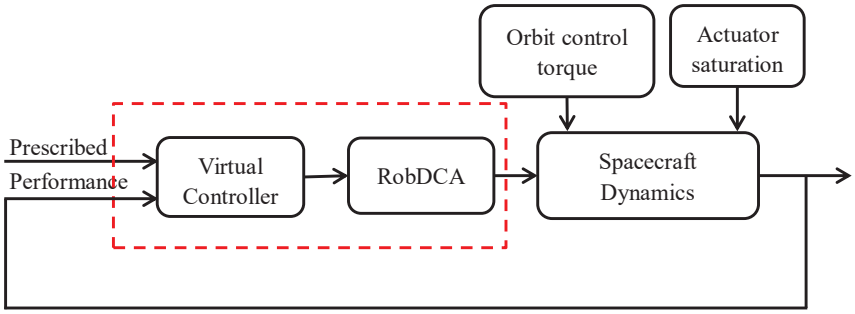

Figure 3: Schematic diagram of the controller design problem description.

surface method is proposed to achieve good stabilization performance for system (19). Meanwhile, a nonlinear disturbance observer is introduced into the control loop to compensate for the effect of the lumped disturbances.

Since there exist significant saturation constraints in low-thrust propulsion, a disturbance-observer-based dynamic surface control (DSC) scheme is designed to generate the total control command with input saturation. The virtual control torque $\boldsymbol{u}_c = [u_{c1}, u_{c2}, u_{c3}]^{\mathrm{T}}$ with constraint is defined as

$$u_{ci} = \begin{cases} u_{i\max}, & \text{if } u_{c0i} > u_{i\max} \\ u_{c0i}, & \text{if } u_{i\min} \le u_{c0i} \le u_{i\max}, \ i = 1,2,3 \\ u_{i\min}, & \text{if } u_{c0i} < u_{i\min} \end{cases} \tag{20}$$

where $\boldsymbol{u}_{c0} = [u_{c01}, u_{c02}, u_{c03}]^{\mathrm{T}}$ is the control command to be designed later, $\boldsymbol{u}_{\max} = [u_{1\max}, u_{2\max}, u_{3\max}]^{\mathrm{T}}$ and $\boldsymbol{u}_{\min} = [u_{1\min}, u_{2\min}, u_{3\min}]^{\mathrm{T}}$ are known maximum and minimum values of the control input, respectively.

In the real problem of thrusters, there exists a limited difference between the desired control input $\boldsymbol{u}_c$ and the nominal control input $\boldsymbol{u}_{c0}$ which is defined as

$$\Delta\boldsymbol{u} = \boldsymbol{u}_c - \boldsymbol{u}_{c0} \tag{21}$$

where $\Delta\boldsymbol{u}$ is bounded, i.e. $\|\Delta\boldsymbol{u}\| \le \varsigma_1$ with a constant $\varsigma_1 \ge 0$ without loss of generality [38].

Define the following change of coordinates

$$\boldsymbol{e}_2 = \boldsymbol{\omega} - \boldsymbol{x}_{2d} \tag{22}$$

$$\boldsymbol{y}_2 = \boldsymbol{x}_{2d} - \bar{\boldsymbol{x}}_2 \tag{23}$$

where $\boldsymbol{e}_2$ is the virtual error surface, $\boldsymbol{x}_{2d}$ and $\bar{\boldsymbol{x}}_2$ are state variable and intermediate control function respectively which will be given later, and $\boldsymbol{y}_2$ denotes the boundary-layer error between $\boldsymbol{x}_{2d}$ and $\bar{\boldsymbol{x}}_2$.

Following the idea of [18, 19, 39], the prescribed performance can be described by the following inequality

$$-\eta_{i,\min}\rho_i(t) < \sigma_i(t) < \eta_{i,\max}\rho_i(t),\ i = 1,2,3,\ \forall t > 0 \tag{24}$$

where $\rho_i(t) : \mathbb{R}^+ \to \mathbb{R}^+$ is formulated as $\rho_i(t) = (\rho_{i0} - \rho_{i\infty})e^{-\gamma_i t} + \rho_{i\infty}$ with $\rho_{i0} > \rho_{i\infty} > 0$, $\gamma_i > 0$, $i = 1,2,3$. ρ_{i0} can be set to fulfill $-\eta_{i,\min}\rho_{i0} < \sigma_1(0) < \eta_{i,\max}\rho_{i0}$, and $\eta_{i,\max}, \eta_{i,\min}$ are positive constants. Here, $\rho_{i0}, \rho_{i\infty}$ denote the initial error bound and the maximum allowed steady error, respectively, and the constant γ_i, which is related to the decreasing rate of $\rho_i(t)$, influences the convergence rate of the attitude.

To achieve the performance in (24), we can transform the constrained attitude into an equivalent unconstrained one, Specifically, we define

$$\sigma_i(t) = \rho_i(t)S[\varepsilon_i(t)],\ i = 1,2,3 \tag{25}$$

in which $\varepsilon_i(t)$ is the transformed error, and the transformed function $S[\varepsilon_i(t)] = (\eta_{i,\max}e^{\varepsilon_i} - \eta_{i,\min}e^{-\varepsilon_i})/(e^{\varepsilon_i} + e^{-\varepsilon_i})$ is smooth and strictly increasing with the following properties: 1) $-\eta_{i,\min} < S(\varepsilon_i) < \eta_{i,\max}$; 2) $\lim_{\varepsilon_i \to +\infty} S(\varepsilon_i) = \eta_{i,\max}$ and $\lim_{\varepsilon_i \to -\infty} S(\varepsilon_i) = -\eta_{i,\min}$.

The function $S(\cdot)$ is strictly monotonically increasing, its inverse function exists, and the transformed error $\varepsilon_i(t)$ can be written as

$$\varepsilon_i(t) = S^{-1}(\lambda_i(t)) = \frac{1}{2}\ln\left(\frac{\eta_{i,\min} + \lambda_i}{\eta_{i,\max} - \lambda_i}\right),\ i = 1,2,3 \tag{26}$$

in which $\lambda_i(t) = \sigma_i(t)/\rho_i(t)$. In addition, the time derivative of the normalized error $\lambda_i(t)$ is

$$\dot{\lambda}_i(t) = \frac{\mathrm{d}(\sigma_i/\rho_i)}{\mathrm{d}t} = \frac{1}{\rho_i}(\dot{\sigma}_i - \lambda_i\dot{\rho}_i) = \frac{1}{\rho_i}(\boldsymbol{I}_{3i}\boldsymbol{G}(\boldsymbol{\sigma})\boldsymbol{\omega} - \lambda_i\dot{\rho}_i), i = 1,2,3 \tag{27}$$

where $\boldsymbol{I}_{31} = [1,0,0]$, $\boldsymbol{I}_{32} = [0,1,0]$ and $\boldsymbol{I}_{33} = [0,0,1]$.

Then the derivative of ε_i is given by

$$\begin{aligned}\dot{\varepsilon}_i &= \frac{\partial S^{-1}}{\partial \lambda_i}\dot{\lambda}_i = \frac{1}{2}\left(\frac{1}{\lambda_i + \eta_{i,\min}} - \frac{1}{\lambda_i - \eta_{i,\max}}\right)\dot{\lambda}_i \\ &= r_i(\boldsymbol{I}_{3i}\boldsymbol{G}(\boldsymbol{\sigma})\boldsymbol{\omega} - \lambda_i\dot{\rho}_i)\end{aligned} \tag{28}$$

in which $r_i = \frac{1}{2\rho_i}(\frac{1}{\lambda_i+\eta_{i,\min}} - \frac{1}{\lambda_i-\eta_{i,\max}})$ can be calculated in terms of σ_i and $\rho_i(t)$ for $i = 1,2,3$. Since $\boldsymbol{r} = \mathrm{diag}\{r_1, r_2, r_3\}$ is a continuous function, there exists a positive constant r_M such that $\|\boldsymbol{r}\| \le r_M$ within a compact set.

Define $\boldsymbol{e}_1(t) = [e_{11}(t), e_{12}(t), e_{13}(t)]^{\mathrm{T}}$, $\boldsymbol{\varepsilon}(t) = [\varepsilon_1(t), \varepsilon_2(t), \varepsilon_3(t)]^{\mathrm{T}}$, $\boldsymbol{\rho} = [\rho_1(t), \rho_2(t), \rho_3(t)]^{\mathrm{T}}$, $\boldsymbol{\lambda} = \mathrm{diag}\{\lambda_1, \lambda_2, \lambda_3\}$ and the following state transformation

$$e_{1i}(t) = \varepsilon_i(t) - \frac{1}{2}\ln\frac{\eta_{i,\min}}{\eta_{i,\max}},\ i = 1, 2, 3 \tag{29}$$

Then we obtain

$$\dot{\boldsymbol{e}}_1(t) = \boldsymbol{r}(\boldsymbol{G}(\boldsymbol{\sigma})\boldsymbol{\omega} - \boldsymbol{\lambda}\dot{\boldsymbol{\rho}}) \tag{30}$$

Remark 2. *We will prove the boundedness of $\boldsymbol{e}_1(t)$ that ensures $\boldsymbol{e}_1(t)$ converges to a neighbourhood of zero. Then according to definition (26) and the transformation (29), $\boldsymbol{\lambda}$ will converge to a neighbourhood of zero. For $\lambda_i(t) = \sigma_i(t)/\rho_i(t)$, $i = 1, 2, 3$, then $\sigma_i(t)$ $(i = 1, 2, 3)$ will converge to zero at a faster rate than $\rho_i(t)$.*

135 In the following, a design process of disturbance-observer-based dynamic surface controller is presented.

Step 1: For (30), it is natural to determine the virtual control law $\bar{\boldsymbol{x}}_2$ in the following form

$$\bar{\boldsymbol{x}}_2 = -(\boldsymbol{r}\boldsymbol{G}(\boldsymbol{\sigma}))^{-1}(k_1\boldsymbol{e}_1 - \boldsymbol{r}\boldsymbol{\lambda}\dot{\boldsymbol{\rho}}) \tag{31}$$

where k_1 is a positive constant. Using the idea of dynamic surface control, we pass $\bar{\boldsymbol{x}}_2$ through a first-order filter with time constant $\tau > 0$ to obtain a filtered virtual control $\boldsymbol{x}_{2d}$:

$$\tau\dot{\boldsymbol{x}}_{2d} + \boldsymbol{x}_{2d} = \bar{\boldsymbol{x}}_2,\ \boldsymbol{x}_{2d}(0) = \bar{\boldsymbol{x}}_2(0) \tag{32}$$

Consider the following augmented Lyapunov function candidate

$$V_1 = \frac{1}{2}\boldsymbol{e}_1^{\mathrm{T}}\boldsymbol{e}_1 \tag{33}$$

then with (31) and the derivative of V_1 along the system (30) is given by

$$\begin{aligned}
\dot{V}_1 &= \boldsymbol{e}_1^{\mathrm{T}}\dot{\boldsymbol{e}}_1 \\
&= \boldsymbol{e}_1^{\mathrm{T}}\boldsymbol{r}(\boldsymbol{G}(\boldsymbol{\sigma})(\boldsymbol{e}_2 + \boldsymbol{x}_{2d}) - \boldsymbol{\lambda}\dot{\boldsymbol{\rho}}) \\
&= \boldsymbol{e}_1^{\mathrm{T}}\boldsymbol{r}(\boldsymbol{G}(\boldsymbol{\sigma})(\boldsymbol{e}_2 + \boldsymbol{y}_2 + \bar{\boldsymbol{x}}_2) - \boldsymbol{\lambda}\dot{\boldsymbol{\rho}}) \\
&= -k_1\boldsymbol{e}_1^{\mathrm{T}}\boldsymbol{e}_1 + \boldsymbol{e}_1^{\mathrm{T}}\boldsymbol{r}\boldsymbol{G}(\boldsymbol{\sigma})(\boldsymbol{e}_2 + \boldsymbol{y}_2)
\end{aligned} \tag{34}$$

Step 2:The control law $\boldsymbol{u}_{c0}$ is designed in this step, the derivative of $\boldsymbol{e}_2$ is

$$\begin{aligned}
\dot{\boldsymbol{e}}_2 &= \dot{\boldsymbol{\omega}} - \dot{\boldsymbol{x}}_{2d} \\
&= \boldsymbol{A} + \boldsymbol{B}\boldsymbol{u}_{c0} + \boldsymbol{\delta} + \boldsymbol{B}\Delta\boldsymbol{u}_c - \dot{\boldsymbol{x}}_{2d}
\end{aligned} \tag{35}$$

where

$$\boldsymbol{A} = -\boldsymbol{J}_0^{-1}\boldsymbol{\omega}^{\times}\boldsymbol{J}_0\boldsymbol{\omega} + \boldsymbol{B}\boldsymbol{u}_t + \boldsymbol{u}_{g0}$$

Design the control input command for system model (30) as

$$\boldsymbol{u}_{c0} = \boldsymbol{B}^{\dagger}[-k_2\boldsymbol{e}_2 - \boldsymbol{G}^{\mathrm{T}}(\boldsymbol{\sigma})\boldsymbol{r}\boldsymbol{e}_1 - k_3\boldsymbol{B}\boldsymbol{\varsigma} - \boldsymbol{A} - \hat{\boldsymbol{\delta}} + \boldsymbol{y}_2/\tau] \tag{36}$$

where

$$\boldsymbol{B}^{\dagger} = \boldsymbol{B}^{\mathrm{T}}(\boldsymbol{B}\boldsymbol{B}^{\mathrm{T}})^{-1} \tag{37}$$

and $\boldsymbol{\varsigma}$ is the output of the following anti-windup saturation compensator

$$\dot{\boldsymbol{\varsigma}} = -k_4\boldsymbol{\varsigma} + \Delta\boldsymbol{u} \tag{38}$$

where k_4 is a positive constant, and $\hat{\boldsymbol{\delta}} = \boldsymbol{\zeta} + \beta\boldsymbol{e}_2$ with a positive constant β and $\boldsymbol{\zeta}$ is the output of the following nonlinear disturbance observer [24]:

$$\dot{\boldsymbol{\zeta}} = -\beta\boldsymbol{\zeta} - \beta[\boldsymbol{A} + \boldsymbol{B}\boldsymbol{u}_c + \boldsymbol{y}_2/\tau + \beta\boldsymbol{e}_2] \tag{39}$$

Now consider the following Lyapunov function candidate

$$V_2 = \frac{1}{2}(\boldsymbol{e}_2^{\mathrm{T}}\boldsymbol{e}_2 + \boldsymbol{\varsigma}^{\mathrm{T}}\boldsymbol{\varsigma} + \tilde{\boldsymbol{\delta}}^{\mathrm{T}}\tilde{\boldsymbol{\delta}}) \tag{40}$$

where $\tilde{\boldsymbol{\delta}} = \boldsymbol{\delta} - \hat{\boldsymbol{\delta}}$, then the derivative of V_2 along the system (35) satisfies

$$\begin{aligned}\dot{V}_2 &= \boldsymbol{e}_2^{\mathrm{T}}\dot{\boldsymbol{e}}_2 + \boldsymbol{\varsigma}^{\mathrm{T}}\dot{\boldsymbol{\varsigma}} + \tilde{\boldsymbol{\delta}}^{\mathrm{T}}\dot{\tilde{\boldsymbol{\delta}}} \\ &= \boldsymbol{e}_2^{\mathrm{T}}(-k_2\boldsymbol{e}_2 - \boldsymbol{G}^{\mathrm{T}}(\boldsymbol{\sigma})\boldsymbol{r}\boldsymbol{e}_1 - k_3\boldsymbol{B}\boldsymbol{\varsigma} + \boldsymbol{B}\Delta\boldsymbol{u}_c + \tilde{\boldsymbol{\delta}}) \\ &\quad - k_4\boldsymbol{\varsigma}^{\mathrm{T}}\boldsymbol{\varsigma} + \boldsymbol{\varsigma}^{\mathrm{T}}\Delta\boldsymbol{u} + \tilde{\boldsymbol{\delta}}^{\mathrm{T}}\dot{\boldsymbol{\delta}} - \beta\tilde{\boldsymbol{\delta}}^{\mathrm{T}}\tilde{\boldsymbol{\delta}}\end{aligned} \tag{41}$$

For the application to the de-tumbling combined spacecraft, the gravity gradient torque $\boldsymbol{u}_g$ is seen as the part of the lumped disturbance. Then attitude dynamics of the combined chaser-target system can be written as

$$\dot{\boldsymbol{\omega}} = -\boldsymbol{J}_0^{-1}\boldsymbol{\omega}^{\times}\boldsymbol{J}_0\boldsymbol{\omega} + \boldsymbol{B}\boldsymbol{u}_c + \boldsymbol{B}\boldsymbol{u}_t + \boldsymbol{\delta}_{\omega} \tag{42}$$

with

$$\begin{aligned}\boldsymbol{\delta}_{\omega} = &-\Delta\tilde{\boldsymbol{J}}\boldsymbol{\omega}^{\times}\boldsymbol{J}\boldsymbol{\omega} - \boldsymbol{J}_0^{-1}\boldsymbol{\omega}^{\times}\Delta\boldsymbol{J}\boldsymbol{\omega} + \Delta\tilde{\boldsymbol{J}}\boldsymbol{u}_c \\ &+ \Delta\tilde{\boldsymbol{J}}\boldsymbol{u}_t + \boldsymbol{J}^{-1}\boldsymbol{u}_g + \boldsymbol{J}^{-1}\boldsymbol{d}\end{aligned}$$

The reduced controller is designed as

$$\boldsymbol{u}_{c0} = \boldsymbol{B}^{\dagger}[-k_2\boldsymbol{\omega} - k_3\boldsymbol{B}\boldsymbol{\varsigma} + \boldsymbol{J}_0^{-1}\boldsymbol{\omega}^{\times}\boldsymbol{J}_0\boldsymbol{\omega} - \boldsymbol{B}\boldsymbol{u}_t - \hat{\boldsymbol{\delta}}_{\omega}] \tag{43}$$

where k_3 is a positive constant, $\hat{\boldsymbol{\delta}}_{\omega} = \boldsymbol{\zeta}_{\omega} + \beta_{\omega}\boldsymbol{\omega}$ is the estimation of $\boldsymbol{\delta}_{\omega}$ with positive constant β_{ω} and ζ is the output of the following nonlinear disturbance observer

$$\dot{\boldsymbol{\zeta}}_{\omega} = -\beta_{\omega}\boldsymbol{\zeta}_{\omega} - \beta_{\omega}[-\boldsymbol{J}_0^{-1}\boldsymbol{\omega}^{\times}\boldsymbol{J}_0\boldsymbol{\omega} + \boldsymbol{B}\boldsymbol{u}_t + \boldsymbol{B}\boldsymbol{u}_c + \beta_{\omega}\boldsymbol{\omega}] \tag{44}$$

3.2. Stability Analysis

The closed-loop attitude dynamics control system of the combined spacecraft with actuator saturation can be expressed as

$$\begin{cases} \dot{\boldsymbol{e}}_1(t) = \boldsymbol{r}(\boldsymbol{G}(\boldsymbol{\sigma})\boldsymbol{\omega} - \boldsymbol{\lambda}\dot{\boldsymbol{\rho}}) \\ \dot{\boldsymbol{e}}_2(t) = \boldsymbol{A} + \boldsymbol{B}\boldsymbol{u}_{c0} + \boldsymbol{B}\Delta\boldsymbol{u}_c + \boldsymbol{\delta}_1 - \dot{\boldsymbol{x}}_{2d} \\ \dot{\boldsymbol{y}}_2 = -\boldsymbol{y}_2/\boldsymbol{\tau} - \dot{\bar{\boldsymbol{x}}}_2 \\ \dot{\boldsymbol{\varsigma}} = -k_4\boldsymbol{\varsigma} + \Delta\boldsymbol{u} \end{cases} \tag{45}$$

Then based on the dynamic surface control theory [40], the following theorem is proposed.

Theorem 1. *Consider the combined spacecraft attitude model with orbit control torque (19). the parameters of the controller (36) satisfy* $2k_4k_2 > 3k_3^2k_5^2$, $2\beta k_2 > 3$, $16k_1 > 3r_M^2\tau$ *with* $k_5 = \|\boldsymbol{B}\|$ *which is the Euclidean norm of the matrix B, then all signals in the resulting closed-loop system are uniformly ultimately bounded, and the attitude* $\boldsymbol{\sigma}$ *converges to a neighborhood of the origin within the prescribed performance bound (24) for all* $t \geq 0$.

Proof. By using tedious but straightforward calculations, we have

$$\left\|\tilde{\bar{\boldsymbol{x}}}_2\right\| \leq \mu(\boldsymbol{e}_1, \boldsymbol{e}_2, \tilde{\boldsymbol{\delta}}, \boldsymbol{y}_2) \tag{46}$$

where μ is a continuous function. The Lyapunov function candidate of the whole attitude control system is taken as

$$V = V_1 + V_2 + V_3 \tag{47}$$

where $V_3 = \frac{1}{2}\boldsymbol{y}_2^{\mathrm{T}}\boldsymbol{y}_2$.

The derivative of V along the system trajectories is given by

$$\begin{aligned}
\dot{V} &= \dot{V}_1 + \dot{V}_2 + \dot{V}_3 \\
&\leq -k_1 \boldsymbol{e}_1^{\mathrm{T}} \boldsymbol{e}_1 + \boldsymbol{e}_1^{\mathrm{T}} \boldsymbol{r} (\boldsymbol{G}(\sigma)(\boldsymbol{e}_2 + \boldsymbol{y}_2) \\
&+ \boldsymbol{e}_2^{\mathrm{T}} (-k_2 \boldsymbol{e}_2 - \boldsymbol{G}^{\mathrm{T}}(\sigma) \boldsymbol{r} \boldsymbol{e}_1 - k_3 \boldsymbol{B} \boldsymbol{\varsigma} + \boldsymbol{B} \Delta \boldsymbol{u}_c + \tilde{\boldsymbol{\delta}}) \\
&- k_4 \boldsymbol{\varsigma}^{\mathrm{T}} \boldsymbol{\varsigma} + \boldsymbol{\varsigma}^{\mathrm{T}} \Delta \boldsymbol{u} + \boldsymbol{y}_2^{\mathrm{T}} (-\boldsymbol{y}_2 / \tau - \dot{\bar{\boldsymbol{x}}}_2) + \tilde{\boldsymbol{\delta}}^{\mathrm{T}} \dot{\boldsymbol{\delta}} - \beta \tilde{\boldsymbol{\delta}}^{\mathrm{T}} \tilde{\boldsymbol{\delta}} \\
&\leq -k_1 \|\boldsymbol{e}_1\|^2 - k_2 \|\boldsymbol{e}_2\|^2 - k_4 \|\boldsymbol{\varsigma}\|^2 - \frac{1}{\tau} \left\|\boldsymbol{y}_2\right\|^2 - \beta \left\|\tilde{\boldsymbol{\delta}}\right\|^2 \\
&+ \|\boldsymbol{e}_1\| \|\boldsymbol{r}\| \|\boldsymbol{G}(\sigma)\| \left\|\boldsymbol{y}_2\right\| + \|\boldsymbol{e}_2\| \left\|\tilde{\boldsymbol{\delta}}\right\| + k_3 k_5 \|\boldsymbol{e}_2\| \|\boldsymbol{\varsigma}\| \\
&+ k_5 \|\boldsymbol{e}_2\| \|\Delta \boldsymbol{u}\| + \|\boldsymbol{\varsigma}\| \|\Delta \boldsymbol{u}\| + |\mu| \left\|\boldsymbol{y}_2\right\| + \left\|\tilde{\boldsymbol{\delta}}\right\| \left\|\dot{\boldsymbol{\delta}}\right\|
\end{aligned} \tag{48}$$

Now consider the set $A = \{\boldsymbol{e}_1, \boldsymbol{e}_2, \tilde{\boldsymbol{\delta}}, \boldsymbol{y}_2 : V \leq p\}$, thus A is a compact set. And for $1/4 \leq \|\boldsymbol{G}(\sigma)\| = \left\|(1 + \boldsymbol{\sigma}^{\mathrm{T}}\boldsymbol{\sigma})/4\right\| \leq 1/2$, (48) can be rewritten as

$$\begin{aligned}
\dot{V} &\leq -k_1 \|\boldsymbol{e}_1\|^2 - k_2 \|\boldsymbol{e}_2\|^2 - k_4 \|\boldsymbol{\varsigma}\|^2 - \beta \left\|\tilde{\boldsymbol{\delta}}\right\|^2 - \frac{1}{\tau} \left\|\boldsymbol{y}_2\right\|^2 \\
&+ (r_M/2) \|\boldsymbol{e}_1\| \left\|\boldsymbol{y}_2\right\| + \|\boldsymbol{e}_2\| \left\|\tilde{\boldsymbol{\delta}}\right\| + k_3 k_5 \|\boldsymbol{e}_2\| \|\boldsymbol{\varsigma}\| \\
&+ k_5 \|\boldsymbol{e}_2\| \|\Delta \boldsymbol{u}\| + \|\boldsymbol{\varsigma}\| \|\Delta \boldsymbol{u}\| + |\mu| \left\|\boldsymbol{y}_2\right\| + \left\|\tilde{\boldsymbol{\delta}}\right\| \left\|\dot{\boldsymbol{\delta}}\right\| \\
&= \sum_{i=1}^{8} \Theta_i
\end{aligned} \tag{49}$$

where

$$\begin{aligned}
\Theta_1 &= -\frac{k_1}{2} \|\boldsymbol{e}_1\|^2 - \frac{k_2}{4} \|\boldsymbol{e}_2\|^2 - \frac{2k_4}{3} \|\boldsymbol{\varsigma}\|^2 \\
&\quad - \frac{2\beta}{3} \left\|\tilde{\boldsymbol{\delta}}\right\|^2 - \frac{2}{3\tau} \left\|\boldsymbol{y}_2\right\|^2, \\
\Theta_2 &= -\frac{k_1}{2} (\|\boldsymbol{e}_1\| - \frac{r_M}{2k_1} \left\|\boldsymbol{y}_2\right\|)^2 + \frac{r_M^2}{8k_1} \left\|\boldsymbol{y}_2\right\|^2, \\
\Theta_3 &= -\frac{k_2}{4} (\|\boldsymbol{e}_2\| - \frac{2k_3 k_5}{k_2} \|\boldsymbol{\varsigma}\|)^2 + \frac{k_3^2 k_5^2}{k_2} \|\boldsymbol{\varsigma}\|^2
\end{aligned}$$

$$
\begin{aligned}
\Theta_4 &= -\frac{k_2}{4}(\|\boldsymbol{e}_2\| - \frac{2}{k_2}\left\|\tilde{\boldsymbol{\delta}}\right\|)^2 + \frac{1}{k_2}\left\|\tilde{\boldsymbol{\delta}}\right\|^2, \\
\Theta_5 &= -\frac{k_2}{4}(\|\boldsymbol{e}_2\| - \frac{2k_5}{k_2}\|\Delta\boldsymbol{u}\|)^2 + \frac{k_5^2}{k_2}\|\Delta\boldsymbol{u}\|^2, \\
\Theta_6 &= -\frac{k_4}{3}(\|\boldsymbol{\varsigma}\| - \frac{3}{2k_4}\|\Delta\boldsymbol{u}\|)^2 + \frac{3}{4k_4}\|\Delta\boldsymbol{u}\|^2, \\
\Theta_7 &= -\frac{\beta}{3}(\left\|\tilde{\boldsymbol{\delta}}\right\| - \frac{3}{2\lambda}\left\|\dot{\boldsymbol{\delta}}\right\|)^2 + \frac{3}{4\beta}\left\|\dot{\boldsymbol{\delta}}\right\|^2, \\
\Theta_8 &= -\frac{1}{3\tau}(\left\|\boldsymbol{y}_2\right\| - \frac{3\tau}{2}|\mu|)^2 + \frac{3\tau}{4}|\mu|^2,
\end{aligned}
$$

then we can have

$$
\begin{aligned}
\dot{V} &\le -\frac{k_1}{2}\|\boldsymbol{e}_1\|^2 - \frac{k_2}{4}\|\boldsymbol{e}_2\|^2 \\
&\quad - (\frac{2k_4}{3} - \frac{k_3^2k_5^2}{k_2})\|\boldsymbol{\varsigma}\|^2 - (\frac{2\beta}{3} - \frac{1}{k_2})\left\|\tilde{\boldsymbol{\delta}}\right\|^2 \\
&\quad - (\frac{2}{3\tau} - \frac{r_M^2}{8k_1})\left\|\boldsymbol{y}_2\right\|^2 + (\frac{k_5^2}{k_2} + \frac{3}{4k_4})\|\Delta\boldsymbol{u}\|^2 \\
&\quad + \frac{3\tau}{4}|\mu|^2 + \frac{3}{4\lambda}\left\|\dot{\boldsymbol{\delta}}\right\|^2 \\
&\le -\gamma V + \epsilon
\end{aligned} \tag{50}
$$

where

$$
\gamma = 2\min\{\frac{k_1}{2}, \frac{k_2}{4}, \frac{2k_4}{3} - \frac{k_3^2k_5^2}{k_2}, \frac{2\beta}{3} - \frac{1}{k_2}, \frac{2}{3\tau} - \frac{r_M^2}{8k_1}\} > 0, \tag{51}
$$

$$
\epsilon = (\frac{k_5^2}{k_2} + \frac{3}{4k_4})\|\Delta\boldsymbol{u}\|^2 + \frac{3\tau}{4}|\mu|^2 + \frac{3}{4\lambda}\left\|\dot{\boldsymbol{\delta}}\right\|^2, \tag{52}
$$

Then according to the comparison principle, we have $V(t) \le V(t_0)e^{-\gamma t} + \frac{1}{\rho}\epsilon$.

Because A is a compact set, there exists a maximum value of $\mu(\boldsymbol{e}_1, \boldsymbol{e}_2, \tilde{\boldsymbol{\delta}}, \boldsymbol{y}_2)$ on A, moreover, $\dot{\boldsymbol{\delta}}$ is assumed as small bounded signal if $\boldsymbol{\delta}$ is viewed as slowly varying signals with respect to the fast dynamics of disturbance observers under large observer gains, then $\epsilon \le \xi$ can be derived with an unknown scalar ξ. For any $V(0) \le p$, if we choose $\gamma p > \xi$, it follows that $\dot{V} < 0$ on $V = p$. Therefore, $V \le p$ is an invariant set, meaning that if $V(0) \le p$, then $V(t) \le p$ for all $t > 0$. Furthermore, assume that $\gamma p = \xi/k_0$, where $0 < k_0 < 1$. It is implied by (50) that, inside the invariant set, $\dot{V} < 0$ for $V \ge p^*$, where $p^* = \xi/\gamma = k_0 p$. Because k_0 can be set as arbitrarily small, p^* can be made small enough. This means that the error surface $\|\boldsymbol{e}_1\|$ and $\|\boldsymbol{e}_2\|$, saturation compensator $\|\boldsymbol{\varsigma}\|$, estimation error $\tilde{\boldsymbol{\delta}}$ and the boundary-layer error $\left\|\boldsymbol{y}_2\right\|$ can be made arbitrarily small ultimately through properly adjusting design parameters as $t \to \infty$.

Furthermore, because the transformed errors $\boldsymbol{e}_1$ is bounded, then the attitude $\boldsymbol{\sigma}(t)$ can be retained with within a set, that is,

$$-\eta_{i\min}\rho_i(t) < \sigma_i(t) < \eta_{i\max}\rho_i(t),\ i = 1, 2, 3,\ \forall t > 0$$

is true [19]. ■

Remark 3. *An increase in γ results in a faster convergence rate. In addition, γ is related to the parameters of the controller, saturation compensator and observer k_1, k_2, k_3, k_4, β and τ. An increase in any of the parameters k_1, k_2, k_4, β or a decrease in k_3, τ lead to an increase in γ and thus a faster convergence rate of attitude.*

Remark 4. *In contrast to the linear disturbance observer in [27] and the terminal sliding mode observer in [38], the observer used to estimated the lumped disturbance in this paper only requires the tuning of one parameter.*

Remark 5. *Using the function $S[\varepsilon_i(t)]$, transforms the problem of guaranteeing the prescribed performance of (24) into the problem of stabilizing the system (45). Since the selection of the controller parameters and system performance have been decoupled, our only concern is to adopt those parameter values that lead to reasonable control effort. This is a critical property as it simplifies the control parameter selection process [19].*

Remark 6. *By introducing the first-order filter (33), the proposed control law does not involve the differentiation of the term $\boldsymbol{G}(\boldsymbol{\sigma})^{-1}$ and thus avoids the 'explosion of complexity' inherent in the backstepping method [29].*

Theorem 2. *Consider the attitude dynamics of the combined chaser-target system in (42). For the detumbling of the combined spacecraft, if the parameter of controller (43) satisfies $8k_2k_4 > 15k_5^2k_3^2$ and $8\beta_\omega k_2 > 15$ with $k_5 = \|\boldsymbol{B}\|$ and all the parameters are positive, the angular velocity $\boldsymbol{\omega}$ is uniformly ultimately bounded.*

Proof. Define the Lyapunov function candidate as

$$V_\omega = \frac{1}{2}(\boldsymbol{\omega}^{\mathrm{T}}\boldsymbol{\omega} + \boldsymbol{\varsigma}^{\mathrm{T}}\boldsymbol{\varsigma} + \tilde{\boldsymbol{\delta}}_\omega^{\mathrm{T}}\tilde{\boldsymbol{\delta}}_\omega)$$

where $\tilde{\boldsymbol{\delta}}_\omega = \boldsymbol{\delta}_\omega - \hat{\boldsymbol{\delta}}_\omega$, then the derivative of V_2 satisfies

$$\begin{aligned}
\dot{V}_\omega &= \boldsymbol{\omega}^{\mathrm{T}}\dot{\boldsymbol{\omega}} + \boldsymbol{\varsigma}^{\mathrm{T}}\dot{\boldsymbol{\varsigma}} + \tilde{\boldsymbol{\delta}}_\omega^{\mathrm{T}}\dot{\tilde{\boldsymbol{\delta}}}_\omega \\
&= \boldsymbol{\omega}^{\mathrm{T}}(-\boldsymbol{J}_0^{-1}\boldsymbol{\omega}^{\times}\boldsymbol{J}_0\boldsymbol{\omega} + \boldsymbol{B}\boldsymbol{u}_c + \boldsymbol{B}\boldsymbol{u}_t + \boldsymbol{\delta}_\omega) \\
&+ \boldsymbol{\varsigma}^{\mathrm{T}}(-k_4\boldsymbol{\varsigma} + \Delta\boldsymbol{u}) + \tilde{\boldsymbol{\delta}}_\omega^{\mathrm{T}}(\dot{\boldsymbol{\delta}}_\omega - \dot{\hat{\boldsymbol{\delta}}}_\omega) \\
&= -k_2\boldsymbol{\omega}^{\mathrm{T}}\boldsymbol{\omega} - k_4\boldsymbol{\varsigma}^{\mathrm{T}}\boldsymbol{\varsigma} - \beta_\omega\tilde{\boldsymbol{\delta}}_\omega^{\mathrm{T}}\tilde{\boldsymbol{\delta}}_\omega - k_3\boldsymbol{\omega}^{\mathrm{T}}\boldsymbol{B}\boldsymbol{\varsigma} \\
&+ \boldsymbol{\omega}^{\mathrm{T}}\tilde{\boldsymbol{\delta}}_\omega + \boldsymbol{\omega}^{\mathrm{T}}\boldsymbol{B}\Delta\boldsymbol{u} + \boldsymbol{\varsigma}^{\mathrm{T}}\Delta\boldsymbol{u} + \tilde{\boldsymbol{\delta}}_\omega^{\mathrm{T}}\dot{\boldsymbol{\delta}}_\omega \\
&\le -k_2\left\|\boldsymbol{\omega}\right\|^2 - k_4\left\|\boldsymbol{\varsigma}\right\|^2 - \beta_\omega\left\|\tilde{\boldsymbol{\delta}}_\omega\right\|^2 + k_3k_5\left\|\boldsymbol{\omega}\right\|\left\|\boldsymbol{\varsigma}\right\| \\
&+ \left\|\boldsymbol{\omega}\right\|\left\|\tilde{\boldsymbol{\delta}}_\omega\right\| + k_5\left\|\boldsymbol{\omega}\right\|\left\|\Delta\boldsymbol{u}\right\| + \left\|\boldsymbol{\varsigma}\right\|\left\|\Delta\boldsymbol{u}\right\| + \left\|\tilde{\boldsymbol{\delta}}_\omega\right\|\left\|\dot{\boldsymbol{\delta}}_\omega\right\| \\
&= \sum_{i=1}^{6}\Phi_i
\end{aligned}$$

where

$$\begin{aligned}
\Phi_1 &= -\frac{2k_2}{5}\left\|\boldsymbol{\omega}\right\|^2 - \frac{2k_4}{3}\left\|\boldsymbol{\varsigma}\right\|^2 - \frac{2\beta_\omega}{3}\left\|\tilde{\boldsymbol{\delta}}_\omega\right\|^2, \\
\Phi_2 &= -\frac{k_2}{5}(\left\|\boldsymbol{\omega}\right\| - \frac{5k_3k_5}{2k_2}\left\|\boldsymbol{\varsigma}\right\|)^2 + \frac{5k_3^2k_5^2}{4k_2}\left\|\boldsymbol{\varsigma}\right\|^2, \\
\Phi_3 &= -\frac{k_2}{5}(\left\|\boldsymbol{\omega}\right\| - \frac{5}{2k_2}\left\|\tilde{\boldsymbol{\delta}}_\omega\right\|)^2 + \frac{5}{4k_2}\left\|\tilde{\boldsymbol{\delta}}_\omega\right\|^2, \\
\Phi_4 &= -\frac{k_2}{5}(\left\|\boldsymbol{\omega}\right\| - \frac{5k_5}{2k_2}\left\|\Delta\boldsymbol{u}\right\|)^2 + \frac{5k_5^2}{4k_2}\left\|\Delta\boldsymbol{u}\right\|^2, \\
\Phi_5 &= -\frac{k_4}{3}(\left\|\boldsymbol{\varsigma}\right\| - \frac{3}{2k_4}\left\|\Delta\boldsymbol{u}\right\|)^2 + \frac{3}{4k_4}\left\|\Delta\boldsymbol{u}\right\|^2, \\
\Phi_6 &= -\frac{\beta_\omega}{3}(\left\|\tilde{\boldsymbol{\delta}}_\omega\right\| - \frac{3}{2\beta_\omega}\left\|\dot{\boldsymbol{\delta}}_\omega\right\|)^2 + \frac{3}{4\beta_\omega}\left\|\dot{\boldsymbol{\delta}}_\omega\right\|^2,
\end{aligned}$$

then we can obtain that

$$\begin{aligned}
\dot{V}_\omega &\le -\frac{2k_2}{5}\left\|\boldsymbol{\omega}\right\|^2 - (\frac{2k_4}{3} - \frac{5k_3^2k_5^2}{4k_2})\left\|\boldsymbol{\varsigma}\right\|^2 - (\frac{2\beta_\omega}{3} - \frac{5}{4k_2})\left\|\tilde{\boldsymbol{\delta}}_\omega\right\|^2 \\
&+ (\frac{5k_5^2}{4k_2} + \frac{3}{4k_4})\left\|\Delta\boldsymbol{u}\right\|^2 + \frac{3}{4\beta_\omega}\left\|\dot{\boldsymbol{\delta}}_\omega\right\|^2 \\
&\le -\gamma_\omega V_\omega + \epsilon_\omega
\end{aligned}$$

where

$$\gamma = 2\min\{\frac{2k_2}{5}, \frac{2k_4}{3} - \frac{5k_3^2k_5^2}{4k_2}, \frac{2\beta_\omega}{3} - \frac{5}{4k_2}\} > 0, \tag{53}$$

$$\epsilon = (\frac{5k_5^2}{4k_2} + \frac{3}{4k_4})\left\|\Delta\boldsymbol{u}\right\|^2 + \frac{3}{4\beta_\omega}\left\|\dot{\boldsymbol{\delta}}_\omega\right\|^2 \tag{54}$$

The rest is similar to the proof in Theorem 1, then the result can be obtained. ■

4. Robust dynamic control allocation

In this section, an approach to map the virtual control to each thruster over a prescribed time interval is presented. The robust dynamic control allocation problem includes saturation constraints suitable for use with low-thrust propulsion. Due to physical limitations on thrusters such as amplitude and rate constraints, it is crucial to redistribute the control efforts among the N thrusters in the frame $\sum O_c$. For simplicity, it is assumed that the physical limitations of the thrusters are the same, which are expressed by [13] and [41]

$$\underline{F} \leq F_i \leq \overline{F}, \ \left|\dot{F}_i\right| \leq F_{\text{rate}}, \ i = 1, 2, \cdots, N \tag{55}$$

where $\underline{F}$ and $\overline{F}$ are the lower and upper constraints of force amplitude, F_{rate} is the maximum actuator rate of the i-th thruster. Then, overall constraints are further specified as

$$\boldsymbol{F}_{\min} \leq \boldsymbol{F} \leq \boldsymbol{F}_{\max} \tag{56}$$

where $\boldsymbol{F}_{\min} = [F_{1\min}, \cdots, F_{N\min}]^{\mathrm{T}}$ and $\boldsymbol{F}_{\max} = [F_{1\max}, \cdots, F_{N\max}]^{\mathrm{T}}$ with $F_{i\min} = \max\{\underline{F}, F_i(t-T) - TF_{\text{rate}}\}$ and $F_{i,\max} = \min\{\overline{F}, F_i(t-T) + TF_{\text{rate}}\}$, T is the sampling time, and $F_i(t-T)$ is the i-th command actuator input in the previous sampling instant.

In this paper, the virtual control torque $\boldsymbol{u}_c \in \mathbb{R}^3$ is designed to specify total attitude control torque. Considering measurement error in the reconfiguration matrix of the N thrusters after capture of target spacecraft, the relationship between the virtual control $\boldsymbol{u}_c$ and the control torque of thrusters $\boldsymbol{F}$ is expressed by

$$\boldsymbol{u}_c = \boldsymbol{A}_c\boldsymbol{F} = (\boldsymbol{A}_{c0} + \Delta\boldsymbol{A}_c)\boldsymbol{F} \tag{57}$$

where $\boldsymbol{A}_{c0}$, $\Delta\boldsymbol{A}_c$ represent the nominal and perturbation matrices of thrusters' configuration matrix, respectively. Without loss of generality, the unknown matrix $\Delta\boldsymbol{A}_c$ is bounded by $\|\Delta\boldsymbol{A}_c\| \leq \kappa$ with κ being a known positive scalar. In this paper, there is no need to determine the exact value of κ since a specific form of $\Delta\boldsymbol{A}_c$ is considered in the following part.

Considering uncertainties in (57), robust dynamic control allocation problem (RobDCA) is formulated as

$$\boldsymbol{F} = \arg\min_{\boldsymbol{F}\in\Omega}\{\|\boldsymbol{F}\|^2_{\boldsymbol{M}_1} + \|\boldsymbol{F}(t) - \boldsymbol{F}(t-T)\|^2_{\boldsymbol{M}_2}\} \tag{58}$$

with

$$\Omega = \arg \min_{\boldsymbol{F}_{\min} \le \boldsymbol{F} \le \boldsymbol{F}_{\max}} \max_{\|\Delta \boldsymbol{A}_c\| \le \kappa} \|\boldsymbol{u}_c - (\boldsymbol{A}_{c0} + \Delta \boldsymbol{A}_c)\boldsymbol{F}\|^2 \tag{59}$$

where $\|\boldsymbol{F}\|^2_{\boldsymbol{M}_1}$ stands for $\boldsymbol{F}^{\mathrm{T}} \boldsymbol{M}_1 \boldsymbol{F}$ and the weighting matrix $\boldsymbol{M}_i = \mathrm{diag}\{m_{i1}, m_{i2}, \cdots, m_{iN}\}$ with $m_{ij} \ge 0$, $i = 1, 2$, $j = 1, 2, \cdots, N$. Furthermore, RobDCA can be rewritten as

$$\boldsymbol{F} = \arg \min_{\boldsymbol{F}_{\min} \le \boldsymbol{F} \le \boldsymbol{F}_{\max}} \{\|\boldsymbol{F}\|^2_{\boldsymbol{M}_1} + \|\boldsymbol{F}(t) - \boldsymbol{F}(t-T)\|^2_{\boldsymbol{M}_2} + \max_{\|\Delta \boldsymbol{A}_c\| \le \kappa} h \|\boldsymbol{u}_c - (\boldsymbol{A}_{c0} + \Delta \boldsymbol{A}_c)\boldsymbol{F}\|^2\} \tag{60}$$

where h is a known positive scalar.

If the rotation matrix $\boldsymbol{R}_{sc}$ is determined, $\boldsymbol{e}_i (i = 1, 2, \cdots, N)$ can be determined. Due to measurement and computational errors when determine the location of the mass center of the combined chaser-target, there must exists uncertainty in the position vector $\boldsymbol{r}_c$ where

$$\boldsymbol{r}_c = \boldsymbol{r}_{c0} + \Delta \boldsymbol{r}_c$$

with $\boldsymbol{r}_{c0} = [r_{c01}, r_{c02}, r_{c03}]^{\mathrm{T}}$ and measurement error $\Delta \boldsymbol{r}_c = [\Delta r_{c1}, \Delta r_{c2}, \Delta r_{c3}]^{\mathrm{T}}$, then the configuration matrix $\boldsymbol{A}_c$ can be denoted as

$$\boldsymbol{A}_c = \boldsymbol{A}_{c0} + \Delta \boldsymbol{A}_c$$

where

$$\boldsymbol{A}_{c0} = [\boldsymbol{a}_{c1}, \boldsymbol{a}_{c2}, \cdots, \boldsymbol{a}_{cN}], \ \Delta \boldsymbol{A}_c = [\Delta \boldsymbol{a}_{c1}, \Delta \boldsymbol{a}_{c2}, \cdots, \Delta \boldsymbol{a}_{cN}]$$

with

$$\boldsymbol{a}_{ci} = \boldsymbol{d}_{ci} \times \boldsymbol{e}_i, \ \Delta \boldsymbol{a}_{ci} = \Delta \boldsymbol{d} \times \boldsymbol{e}_i, \ i = 1, 2, \cdots, N$$

and

$$\Delta \boldsymbol{d} = -\boldsymbol{R}_{sc} \Delta \boldsymbol{r}_c, \ \boldsymbol{d}_{ci} = \boldsymbol{R}_{sc}(\boldsymbol{d}_{si} - \boldsymbol{r}_{c0}), \ i = 1, 2, \cdots, N$$

Assume that

$$\boldsymbol{R}_{sc} = \begin{bmatrix} r_{11} & r_{12} & r_{13} \\ r_{21} & r_{22} & r_{23} \\ r_{31} & r_{32} & r_{33} \end{bmatrix}, \ \Delta \boldsymbol{r}_c = \begin{bmatrix} \Delta r_{c1} \\ \Delta r_{c2} \\ \Delta r_{c3} \end{bmatrix}, \ \boldsymbol{e}_i = \begin{bmatrix} e_{1i} \\ e_{2i} \\ e_{3i} \end{bmatrix}$$

for $i = 1, 2, \cdots, N$. Then $\Delta \boldsymbol{a}_{ci}$ can be written as

$$\begin{aligned}\Delta \boldsymbol{a}_{ci} &= \Delta \boldsymbol{d} \times \boldsymbol{e}_i = -(\boldsymbol{R}_{sc} \Delta \boldsymbol{r}_c) \times \boldsymbol{e}_i \\ &= \Delta r_{c1} \begin{bmatrix} e_{2i} r_{31} - e_{3i} r_{21} \\ e_{3i} r_{11} - e_{1i} r_{31} \\ e_{1i} r_{21} - e_{2i} r_{11} \end{bmatrix} + \Delta r_{c2} \begin{bmatrix} e_{2i} r_{32} - e_{3i} r_{22} \\ e_{3i} r_{12} - e_{1i} r_{32} \\ e_{1i} r_{22} - e_{2i} r_{12} \end{bmatrix} + \Delta r_{c3} \begin{bmatrix} e_{2i} r_{33} - e_{3i} r_{23}) \\ e_{3i} r_{13} - e_{1i} r_{33} \\ e_{1i} r_{23} - e_{2i} r_{13} \end{bmatrix}\end{aligned}$$

then $\Delta \boldsymbol{A}_c$ can be represented as

$$\Delta \boldsymbol{A}_c = \Delta r_{c1} A_{c1} + \Delta r_{c2} A_{c2} + \Delta r_{c3} A_{c3} \tag{61}$$

with

$$A_{c1} = \begin{bmatrix} e_{21} r_{31} - e_{31} r_{21} & \cdots & e_{2,N} r_{31} - e_{3,N} r_{21} \\ e_{31} r_{11} - e_{11} r_{31} & \cdots & e_{3,N} r_{11} - e_{1,N} r_{31} \\ e_{11} r_{21} - e_{21} r_{11} & \cdots & e_{1,N} r_{21} - e_{2,N} r_{11} \end{bmatrix}_{3 \times N}$$

$$A_{c2} = \begin{bmatrix} e_{21} r_{32} - e_{31} r_{22} & \cdots & e_{2,N} r_{32} - e_{3,N} r_{22} \\ e_{31} r_{12} - e_{11} r_{32} & \cdots & e_{3,N} r_{12} - e_{1,N} r_{32} \\ e_{11} r_{22} - e_{21} r_{12} & \cdots & e_{1,N} r_{22} - e_{2,N} r_{12} \end{bmatrix}_{3 \times N}$$

$$A_{c3} = \begin{bmatrix} e_{21} r_{33} - e_{31} r_{23}) & \cdots & e_{2,N} r_{33} - e_{3,N} r_{23}) \\ e_{31} r_{13} - e_{11} r_{33} & \cdots & e_{3,N} r_{13} - e_{1,N} r_{33} \\ e_{11} r_{23} - e_{21} r_{13} & \cdots & e_{1,N} r_{23} - e_{2,N} r_{13} \end{bmatrix}_{3 \times N}$$

Without loss of generality, we assume that $\Delta \boldsymbol{r}_c$ satisfies that $\Delta_i^- \leq \Delta r_{ci} \leq \Delta_i^+$. Now define

$$\Delta_I = \{\Delta r_c | \Delta r_{ci} \in [\Delta_i^-, \Delta_i^+], i = 1, 2, 3\}$$

then the RobDCA problem (59) can be transformed to the following form:

$$\boldsymbol{F} = \arg \min_{\boldsymbol{F}_{\min} \leq \boldsymbol{F} \leq \boldsymbol{F}_{\max}} \max_{\Delta r_c \in \Delta_I} \{ ||\boldsymbol{F}||^2_{\boldsymbol{M}_1} + ||\boldsymbol{F}(t) - \boldsymbol{F}(t-T)||^2_{\boldsymbol{M}_2} + h \, ||\boldsymbol{u}_c - A_c(\Delta r_{ci}) \boldsymbol{F}||^2 \} \tag{62}$$

190 and the following result can be obtained.

Theorem 3. *If $\Delta \boldsymbol{r}_c \in \Delta_I$, the RobDCA problem has an optimal solution if the following is solved for any $\Delta \boldsymbol{r}_c \in \Delta_E$*

$$\min_F \Upsilon$$

s.t.

$$\Upsilon_1 + \Upsilon_2 + \Upsilon_3 - \Upsilon < 0 \tag{63}$$

$$\begin{bmatrix} -I & \boldsymbol{M}_1^{1/2}\boldsymbol{F} \\ (\boldsymbol{M}_1^{1/2}\boldsymbol{F})^{\mathrm{T}} & -\Upsilon_1 I \end{bmatrix} < 0 \tag{64}$$

$$\begin{bmatrix} -I & \boldsymbol{M}_2^{1/2}(\boldsymbol{F}(t) - \boldsymbol{F}(t-T)) \\ (\boldsymbol{M}_2^{1/2}(\boldsymbol{F}(t) - \boldsymbol{F}(t-T)))^{\mathrm{T}} & -\Upsilon_2 I \end{bmatrix} < 0$$

$$\begin{bmatrix} -I & \sqrt{h}(\boldsymbol{u}_c - A_c(\Delta r_{ci})\boldsymbol{F}) \\ \sqrt{h}(\boldsymbol{u}_c - A_c(\Delta r_{ci})\boldsymbol{F})^{\mathrm{T}} & -\Upsilon_3 I \end{bmatrix} < 0 \tag{65}$$

$$\begin{bmatrix} \boldsymbol{b}_1^{\mathrm{T}}(\boldsymbol{F}_{\min} - \boldsymbol{F}) & 0 & \cdots & 0 \\ 0 & \boldsymbol{b}_2^{\mathrm{T}}(\boldsymbol{F}_{\min} - \boldsymbol{F}) & \cdots & 0 \\ \vdots & \vdots & \ddots & \vdots \\ 0 & 0 & \cdots & \boldsymbol{b}_N^{\mathrm{T}}(\boldsymbol{F}_{\min} - \boldsymbol{F}) \end{bmatrix} < 0 \tag{66}$$

$$\begin{bmatrix} \boldsymbol{b}_1^{\mathrm{T}}(\boldsymbol{F} - \boldsymbol{F}_{\max}) & 0 & \cdots & 0 \\ 0 & \boldsymbol{b}_2^{\mathrm{T}}(\boldsymbol{F} - \boldsymbol{F}_{\max}) & \cdots & 0 \\ \vdots & \vdots & \ddots & \vdots \\ 0 & 0 & \cdots & \boldsymbol{b}_N^{\mathrm{T}}(\boldsymbol{F} - \boldsymbol{F}_{\max}) \end{bmatrix} < 0 \tag{67}$$

where $\Upsilon > 0, \Upsilon_1 > 0, \Upsilon_2 > 0, \Upsilon_3 > 0, \boldsymbol{b}_i (i = 1, 2, \cdots, N)$ *are unit column vectors and satisfy* $[\boldsymbol{b}_1, \boldsymbol{b}_2, \cdots, \boldsymbol{b}_N] = \boldsymbol{I}_N$, *and* $\Delta_E = \{\Delta \boldsymbol{r}_c | \Delta r_{ci} = \Delta_i^- \text{ or } \Delta_i^+, i = 1, 2, 3\}$

Proof. Denote

$$\begin{aligned} \Upsilon_1 &= \|\boldsymbol{F}\|_{\boldsymbol{M}_1}^2, \\ \Upsilon_2 &= \|\boldsymbol{F}(t) - \boldsymbol{F}(t-T)\|_{\boldsymbol{M}_2}^2, \\ \Upsilon_3 &= h\,\|\boldsymbol{u}_c - A_c(\Delta r_{ci})\boldsymbol{F}\|^2 \end{aligned}$$

To ensure

$$\max_{\Delta r_c \in \Delta_I} \{\|\boldsymbol{F}\|_{\boldsymbol{M}_1}^2 + \|\boldsymbol{F}(t) - \boldsymbol{F}(t-T)\|_{\boldsymbol{M}_2}^2 + h\,\|\boldsymbol{u}_c - A_c(\Delta r_{ci})\boldsymbol{F}\|^2\} < \Upsilon$$

it holds if

$$\Upsilon_1 + \Upsilon_2 + \Upsilon_3 < \Upsilon$$

and

$$\begin{aligned} \boldsymbol{F}^{\mathrm{T}}\boldsymbol{M}_1\boldsymbol{F} &< \Upsilon_1, \\ (\boldsymbol{F}(t)-\boldsymbol{F}(t-T))^{\mathrm{T}}\boldsymbol{M}_2(\boldsymbol{F}(t)-\boldsymbol{F}(t-T)) &< \Upsilon_2, \\ h(\boldsymbol{u}_c - A_c(\Delta r_{ci})\boldsymbol{F})^{\mathrm{T}}(\boldsymbol{u}_c - A_c(\Delta r_{ci})\boldsymbol{F}) &< \Upsilon_3 \end{aligned} \tag{68}$$

Using the Schur complement Lemma, (68) is equal to

$$\begin{bmatrix} -I & \boldsymbol{M}_1^{1/2}\boldsymbol{F} \\ (\boldsymbol{M}_1^{1/2}\boldsymbol{F})^{\mathrm{T}} & -\Upsilon_1 I \end{bmatrix} < 0$$

$$\begin{bmatrix} -I & \boldsymbol{M}_2^{1/2}(\boldsymbol{F}(t)-\boldsymbol{F}(t-T)) \\ (\boldsymbol{M}_2^{1/2}(\boldsymbol{F}(t)-\boldsymbol{F}(t-T)))^{\mathrm{T}} & -\Upsilon_2 I \end{bmatrix} < 0$$

$$\begin{bmatrix} -I & \sqrt{h}(\boldsymbol{u}_c - A_c(\Delta r_{ci})\boldsymbol{F}) \\ \sqrt{h}(\boldsymbol{u}_c - A_c(\Delta r_{ci})\boldsymbol{F})^{\mathrm{T}} & -\Upsilon_3 I \end{bmatrix} < 0$$

for $\Delta r_c \in \Delta_I$, then according to Corollary 4.3.1 in [42], (65) is obtained.

To add the constraint to $\boldsymbol{F}$, we have

$$\boldsymbol{F}_{\min} < \boldsymbol{F} < \boldsymbol{F}_{\max} \Longleftrightarrow$$

$$\begin{bmatrix} F_{1\min} \\ F_{2\min} \\ \vdots \\ F_{N\min} \end{bmatrix} < \begin{bmatrix} F_1 \\ F_2 \\ \vdots \\ F_N \end{bmatrix} < \begin{bmatrix} F_{1\max} \\ F_{2\max} \\ \vdots \\ F_{N\max} \end{bmatrix} \tag{69}$$

then rewrite left side of (69) as:

$$\begin{bmatrix} F_{1\min} \\ F_{2\min} \\ \vdots \\ F_{N\min} \end{bmatrix} < \begin{bmatrix} F_1 \\ F_2 \\ \vdots \\ F_N \end{bmatrix} \Longleftrightarrow$$

$$\begin{bmatrix} F_{1\min}-F_1 & 0 & \cdots & 0 \\ 0 & F_{2\min}-F_2 & \cdots & 0 \\ \vdots & \vdots & \ddots & \vdots \\ 0 & 0 & \cdots & F_{N\min}-F_N \end{bmatrix} < 0 \Longleftrightarrow$$

$$\begin{bmatrix} \boldsymbol{b}_1^{\mathrm{T}}(\boldsymbol{F}_{\min}-\boldsymbol{F}) & 0 & \cdots & 0 \\ 0 & \boldsymbol{b}_2^{\mathrm{T}}(\boldsymbol{F}_{\min}-\boldsymbol{F}) & \cdots & 0 \\ \vdots & \vdots & \ddots & \vdots \\ 0 & 0 & \cdots & \boldsymbol{b}_N^{\mathrm{T}}(\boldsymbol{F}_{\min}-\boldsymbol{F}) \end{bmatrix}$$

Thus (66) can be obtained, by the same way, we can also get (67). ■

5. Simulation and analysis

To study the effectiveness of the proposed disturbance-observer based dynamic surface control scheme with prescribed performance and the RobDCA strategy, the combined spacecraft system consisting of two 12U CubeSats and one 3-DOF space manipulator is considered, which is shown in Figure 4. The dynamic parameters of the combined spacecraft system are shown in Table 1. In the Table 1, m_s, m_t and m_{li} ($i = 1,2,3$) are the mass of chaser spacecraft, target spacecraft and ith link of manipulator respectively; $\boldsymbol{J}_s$, $\boldsymbol{J}_t$ and $\boldsymbol{J}_{li}$ ($i = 1,2,3$) are the inertia matrix of the chaser spacecraft, target spacecraft and the ith link of manipulator respectively; $\boldsymbol{p}_s$, $\boldsymbol{p}_t$, $\boldsymbol{R}_{sc}$ and $\boldsymbol{R}_{tc}$ are the centroid position vector, attitude rotation matrix of chaser spacecraft and target spacecraft respectively; $\boldsymbol{p}_{li}$ and $\boldsymbol{R}_{li}(i = 1,2,3)$ are the centroid position vector and attitude rotation matrix of the ith link of manipulator respectively. Then according to the result in [32], the nominal inertia matrix of the combined spacecraft can be computed as

$$\begin{aligned} \boldsymbol{J}_0 = {} & \boldsymbol{R}_{sc}\boldsymbol{J}_s\boldsymbol{R}_{sc}^{\mathrm{T}} + \mathrm{m}_s[(\boldsymbol{p}_s^{\mathrm{T}}\boldsymbol{p}_s)\boldsymbol{I}_3 - \boldsymbol{p}_s\boldsymbol{p}_s^{\mathrm{T}}] \\ & + \boldsymbol{R}_{tc}\boldsymbol{J}_t\boldsymbol{R}_{tc}^{\mathrm{T}} + \mathrm{m}_t[(\boldsymbol{p}_t^{\mathrm{T}}\boldsymbol{p}_t)\boldsymbol{I}_3 - \boldsymbol{p}_t\boldsymbol{p}_t^{\mathrm{T}}] \\ & + \sum_{i=1}^{3}\left\{\boldsymbol{R}_{li}\boldsymbol{J}_{li}\boldsymbol{R}_{li}^{T} + \mathrm{m}_{li}[(\boldsymbol{p}_{li}^{\mathrm{T}}\boldsymbol{p}_{li})\boldsymbol{I}_3 - \boldsymbol{p}_{li}\boldsymbol{p}_{li}^{\mathrm{T}}]\right\} \end{aligned} \tag{70}$$

Thus we can get $\boldsymbol{J}_0 = \mathrm{diag}\{0.49019, 1.2089, 1.2916\}\,\mathrm{kg{\cdot}m^2}$ and the inertia uncertainty is set as $\Delta\boldsymbol{J} = 0.1\boldsymbol{J}_0$.

An attitude control system with 12 thrusters and orbit control torque is considered in this paper, which induced by the mis-alignment of the chaser orbital thruster with the centre-of-mass of the combined system is shown in Figure 5. The position vectors and orientation vectors of the thrusters before the target spacecraft has been captured expressed in the body frame of chaser spacecraft $\sum O_s$ are defined in Table 2. And the magnitude of the orbit control force f_0 is defined as $f_0 = 5 \times 10^{-3}$ N, the position vector $\boldsymbol{d}_{s0}$ and the unit orientation vector $\boldsymbol{e}_{s0}$ expressed in the frame $\sum O_s$ are defined as

$$\boldsymbol{d}_{s0} = [0, 0, -0.1]^{\mathrm{T}}\ \mathrm{m},\ \boldsymbol{e}_{s0} = [0, 0, 1]^{\mathrm{T}}$$

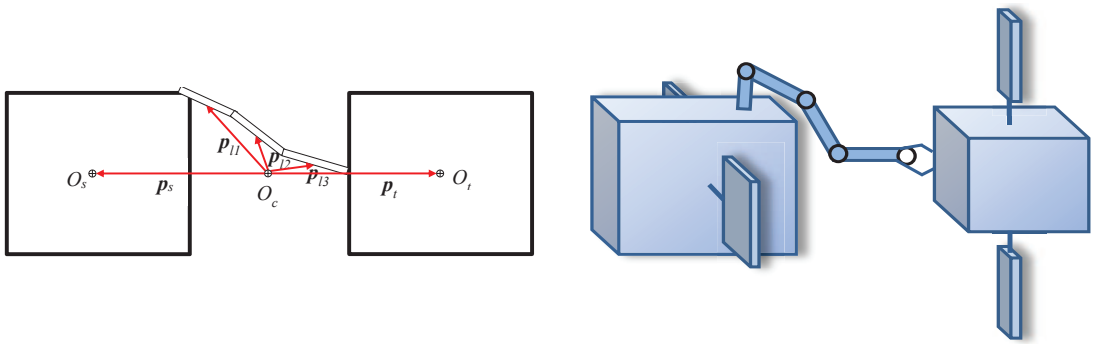

Figure 4: Model of the docked spacecraft system.

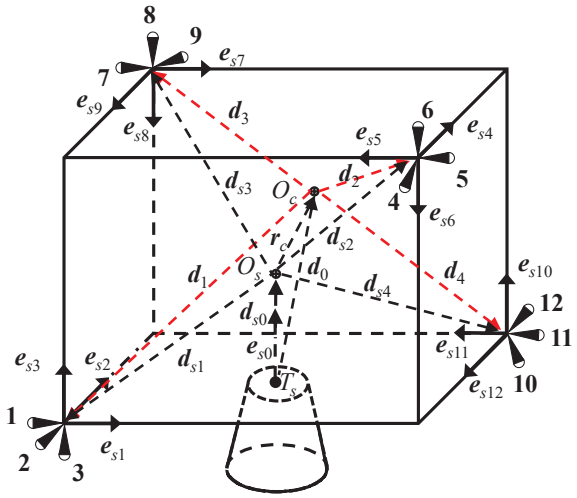

Figure 5: 12 thrusters with orbit control torque

The rotation matrix $\boldsymbol{R}_{sc}$ is set as

$$\boldsymbol{R}_{sc} = \begin{bmatrix} 0.63708 & 0.63708 & -0.43388 \\ -0.87855 & 0.61925 & 0.78026 \\ 0.76577 & -0.45897 & 0.45048 \end{bmatrix}$$

and the vector $\boldsymbol{r}_c$ is defined as $\boldsymbol{r}_c = [0.05, 0.05, 0.05]^{\mathrm{T}}$ m. Then the position vector $\boldsymbol{d}_0$ and the unit orientation vector $\boldsymbol{e}_0$ expressed in frame $\sum O_c$ are

$$\boldsymbol{d}_0 = \boldsymbol{R}_{sc}(\boldsymbol{d}_{s0} - \boldsymbol{r}_c) = [0.00137, -0.14361, -0.08291]^{\mathrm{T}} \text{ m}$$

$$\boldsymbol{e}_0 = \boldsymbol{R}_{sc}\boldsymbol{e}_{s0} = [-0.43388, 0.78026, 0.45048]^{\mathrm{T}}$$

We can also get

$$\boldsymbol{A}_t = \boldsymbol{d}_0 \times \boldsymbol{e}_0 = [0, 0.03536, -0.06124]^{\mathrm{T}},$$

and the orbit control torque

$$\boldsymbol{u}_t = f_0 \boldsymbol{A}_t = \left[0, 1.77 \times 10^{-4}, -3.06 \times 10^{-4}\right]^{\mathrm{T}} \ \mathrm{Nm}$$

Table 1 Dynamic parameters of combined spacecraft system

Body	Parameter	Unit	Value
12U CubeSat	$\mathrm{m}_s(\mathrm{m}_t)$	kg	10
	$\boldsymbol{J}_s(\boldsymbol{J}_t)$	kg·m^2	diag{0.2666, 0.26, 0.1666}
	$\boldsymbol{p}_s$	m	[−0.2; 0; 0]
	$\boldsymbol{p}_t$	m	[0.2; 0; 0]
Link1	m_{l1}	kg	0.17
	$\boldsymbol{J}_{l1}$	kg·m^2	diag{$5 \times 10^{-5}, 4.5 \times 10^{-4}, 4.5 \times 10^{-4}$}
	$\boldsymbol{p}_{l1}$	m	[−0.05; −0.02; 0.05]
Link2	m_{l2}	kg	0.17
	$\boldsymbol{J}_{l2}$	kg·m^2	diag{$5 \times 10^{-5}, 4.5 \times 10^{-4}, 4.5 \times 10^{-4}$}
	$\boldsymbol{p}_{l2}$	m	[−0.01; −0.05; 0.03]
Link3	m_{l3}	kg	0.17
	$\boldsymbol{J}_{l1}$	kg·m^2	diag{$5 \times 10^{-5}, 4.5 \times 10^{-4}, 4.5 \times 10^{-4}$}
	$\boldsymbol{p}_{l3}$	m	[0.03; 0; 0.01]

The rotation matrix $\boldsymbol{R}_{sc}$ is set as

$$\boldsymbol{R}_{sc} = \begin{bmatrix} 0.63708 & 0.63708 & -0.43388 \\ -0.87855 & 0.61925 & 0.78026 \\ 0.76577 & -0.45897 & 0.45048 \end{bmatrix}$$

and the vector $\boldsymbol{r}_c$ is defined as $\boldsymbol{r}_c = [0.05, 0.05, 0.05]^{\mathrm{T}}$ m. Then the position vector $\boldsymbol{d}_0$ and the unit orientation vector $\boldsymbol{e}_0$ expressed in frame $\sum O_c$ are

$$\boldsymbol{d}_0 = \boldsymbol{R}_{sc}(\boldsymbol{d}_{s0} - \boldsymbol{r}_c) = [0.00137, -0.14361, -0.08291]^{\mathrm{T}} \ \mathrm{m}$$

$$\boldsymbol{e}_0 = \boldsymbol{R}_{sc}\boldsymbol{e}_{s0} = [-0.43388, 0.78026, 0.45048]^{\mathrm{T}}$$

We can also get

$$\boldsymbol{A}_t = \boldsymbol{d}_0 \times \boldsymbol{e}_0 = [0, 0.03536, -0.06124]^{\mathrm{T}},$$

and the orbit control torque

$$\boldsymbol{u}_t = f_0 \boldsymbol{A}_t = \left[0, 1.77 \times 10^{-4}, -3.06 \times 10^{-4}\right]^{\mathrm{T}} \text{ Nm}$$

And according to the equation (8) and (9), the position vectors and orientation vectors of the thrusters after the target spacecraft has been captured expressed in the body frame of chaser spacecraft $\sum O_c$ are shown in Table 3.

Table 2 The mounted positions and vectors of the thrusters in the frame $\sum O_s$

Thruster i	Position $\boldsymbol{d}_{si}$(m)	Orientation $\boldsymbol{e}_{si}$
1	$[0.1, -0.1, 0.1]^{\mathrm{T}}$	$[0, 1, 0]^{\mathrm{T}}$
2	$[0.1, -0.1, 0.1]^{\mathrm{T}}$	$[-1, 0, 0]^{\mathrm{T}}$
3	$[0.1, -0.1, 0.1]^{\mathrm{T}}$	$[0, 0, 1]^{\mathrm{T}}$
4	$[0.1, 0.1, 0.1]^{\mathrm{T}}$	$[-1, 0, 0]^{\mathrm{T}}$
5	$[0.1, 0.1, 0.1]^{\mathrm{T}}$	$[0, -1, 0]^{\mathrm{T}}$
6	$[0.1, 0.1, 0.1]^{\mathrm{T}}$	$[0, 0, -1]^{\mathrm{T}}$
7	$[-0.1, -0.1, 0.1]^{\mathrm{T}}$	$[0, 1, 0]^{\mathrm{T}}$
8	$[-0.1, -0.1, 0.1]^{\mathrm{T}}$	$[0, 0, -1]^{\mathrm{T}}$
9	$[-0.1, -0.1, 0.1]^{\mathrm{T}}$	$[1, 0, 0]^{\mathrm{T}}$
10	$[-0.1, 0.1, -0.1]^{\mathrm{T}}$	$[0, 0, 1]^{\mathrm{T}}$
11	$[-0.1, 0.1, -0.1]^{\mathrm{T}}$	$[0, -1, 0]^{\mathrm{T}}$
12	$[-0.1, 0.1, -0.1]^{\mathrm{T}}$	$[1, 0, 0]^{\mathrm{T}}$

Based on (13) and Table 3, we can also get the configuration matrix in the frame $\sum O_c$

$$\boldsymbol{A}_c = [\boldsymbol{a}_1, \boldsymbol{a}_2, \cdots, \boldsymbol{a}_{12}]$$

with

$$\boldsymbol{a}_1 = \begin{bmatrix} -0.05355 \\ 0.04341 \\ -0.01576 \end{bmatrix}, \boldsymbol{a}_2 = \begin{bmatrix} 0.03323 \\ -0.14800 \\ -0.04462 \end{bmatrix}, \boldsymbol{a}_3 = \begin{bmatrix} -0.12742 \\ -0.01778 \\ -0.09192 \end{bmatrix}$$

$$\boldsymbol{a}_4 = \begin{bmatrix} -0.05355 \\ 0.00805 \\ 0.04547 \end{bmatrix}, \boldsymbol{a}_5 = \begin{bmatrix} 0.05355 \\ -0.04341 \\ 0.01576 \end{bmatrix}, \boldsymbol{a}_6 = \begin{bmatrix} 0 \\ 0.03536 \\ -0.06124 \end{bmatrix}$$

$$\boldsymbol{a}_7 = \begin{bmatrix} 0.03323 \\ -0.11265 \\ -0.10586 \end{bmatrix}, \boldsymbol{a}_8 = \begin{bmatrix} 0 \\ -0.10607 \\ 0.18371 \end{bmatrix}, \boldsymbol{a}_9 = \begin{bmatrix} -0.03323 \\ 0.14800 \\ -0.04462 \end{bmatrix}$$

$$\boldsymbol{a}_{10} = \begin{bmatrix} 0.12742 \\ 0.08850 \\ -0.03056 \end{bmatrix}, \boldsymbol{a}_{11} = \begin{bmatrix} -0.16065 \\ 0.13022 \\ -0.04729 \end{bmatrix}, \boldsymbol{a}_{12} = \begin{bmatrix} -0.07387 \\ -0.13190 \\ 0.04632 \end{bmatrix}$$

The low-thrust propulsion FEEP (field emission electric propulsion) [43] is selected in this paper and the limitation on thruster is given as $0 \leq F_i \leq 3.75\times10^{-3}$ N with $i = 1, 2, \cdots, 12$ [43]. The thrusters are assumed to have a continuous thrust force. We set the limitation on $\boldsymbol{u}$ is $\boldsymbol{u}_{\max} = [1.5\times10^{-3}, 1.5\times10^{-3}, 1.5\times10^{-3}]^{\mathrm{T}}$ Nm, $\boldsymbol{u}_{\min} = [-1.5\times10^{-3}, -1.5\times10^{-3}, -1.5\times10^{-3}]^{\mathrm{T}}$ Nm (Note that $\boldsymbol{u}_{\max}$ and $\boldsymbol{u}_{\min}$ are selected such that actuator $\boldsymbol{F}$ is obtained satisfying $\boldsymbol{A}_c\boldsymbol{F} = \boldsymbol{u}$ and $0 \leq F_i \leq 3.75\times10^{-3}$).

Table 3 The mounted positions and vectors of the thrusters in the frame $\sum O_c$

Thruster i	Position $\boldsymbol{d}_i$(m)	Orientation $\boldsymbol{e}_i$
1	$\begin{bmatrix} -0.08540 & -0.05827 & 0.12966 \end{bmatrix}^{\mathrm{T}}$	$\begin{bmatrix} 0.63708 & 0.61925 & -0.45897 \end{bmatrix}^{\mathrm{T}}$
2	$\begin{bmatrix} -0.08540 & -0.05827 & 0.12966 \end{bmatrix}^{\mathrm{T}}$	$\begin{bmatrix} -0.63708 & 0.08785 & -0.76577 \end{bmatrix}^{\mathrm{T}}$
3	$\begin{bmatrix} -0.08540 & -0.05827 & 0.12966 \end{bmatrix}^{\mathrm{T}}$	$\begin{bmatrix} -0.43388 & 0.78026 & 0.45048 \end{bmatrix}^{\mathrm{T}}$
4	$\begin{bmatrix} 0.04201 & 0.06558 & 0.03786 \end{bmatrix}^{\mathrm{T}}$	$\begin{bmatrix} -0.63708 & 0.08785 & -0.76577 \end{bmatrix}^{\mathrm{T}}$
5	$\begin{bmatrix} 0.04201 & 0.06558 & 0.03786 \end{bmatrix}^{\mathrm{T}}$	$\begin{bmatrix} -0.63708 & -0.61925 & 0.45897 \end{bmatrix}^{\mathrm{T}}$
6	$\begin{bmatrix} 0.04201 & 0.06558 & 0.03786 \end{bmatrix}^{\mathrm{T}}$	$\begin{bmatrix} 0.43388 & -0.78026 & -0.45048 \end{bmatrix}^{\mathrm{T}}$
7	$\begin{bmatrix} -0.21282 & -0.04070 & -0.023500 \end{bmatrix}^{\mathrm{T}}$	$\begin{bmatrix} 0.63708 & 0.61925 & -0.45897 \end{bmatrix}^{\mathrm{T}}$
8	$\begin{bmatrix} -0.21282 & -0.04070 & -0.023500 \end{bmatrix}^{\mathrm{T}}$	$\begin{bmatrix} 0.43388 & -0.78026 & -0.45048 \end{bmatrix}^{\mathrm{T}}$
9	$\begin{bmatrix} -0.21282 & -0.04070 & -0.023500 \end{bmatrix}^{\mathrm{T}}$	$\begin{bmatrix} 0.63708 & -0.08785 & 0.76577 \end{bmatrix}^{\mathrm{T}}$
10	$\begin{bmatrix} 0.00137 & -0.072900 & -0.02054 \end{bmatrix}^{\mathrm{T}}$	$\begin{bmatrix} -0.43388 & 0.78026 & 0.45048 \end{bmatrix}^{\mathrm{T}}$,
11	$\begin{bmatrix} 0.00137 & -0.072900 & -0.02054 \end{bmatrix}^{\mathrm{T}}$	$\begin{bmatrix} -0.63708 & -0.61925 & 0.45897 \end{bmatrix}^{\mathrm{T}}$
12	$\begin{bmatrix} 0.00137 & -0.072900 & -0.02054 \end{bmatrix}^{\mathrm{T}}$	$\begin{bmatrix} 0.63708 & -0.08785 & 0.76577 \end{bmatrix}^{\mathrm{T}}$

Remark 7. *In the simulation, a 12U CubeSat is used and its parameters presented in Table 1 are in the typical order of magnitude, for example see [22], [23] and [43]. The positions and vectors of the thrusters in the body frame presented in Table 2 are selected according to the parameters in [11]. The robotic arms are selected based on the parameters in [11] and scaled to the size of the 12U CubeSat (Cubesat robotic arms have not been developed yet). And the magnitudes of the control torque and thruster force are based on [43]. In short, all the parameters used are selected based on the actual physical system.*

Both de-tumbling of the combined spacecraft and the performance of a large angle slew maneuver are investigated. In each case, simulation with PD controller (PD) is used to show the superiority of with the proposed prescribed-performance based dynamic surface control (DSC+PPC). Then, the differential equations related to the mathematical model of attitude stabilization control system of combined spacecraft, the control laws, the nonlinear disturbance observer and saturation compensator were integrated using a fixed-step Runge–Kutta solver (0.1 s).

5.1. De-tumbling of a combined spacecraft CubeSat

In that case, the initial angular velocity of the combined spacecraft is $\boldsymbol{\omega}(0) = [0.45, 0.52, 0.55]^{\mathrm{T}}$ rad/s and the initial attitude MRPs of the combined spacecraft is set to be zero. Also, we assume that de-tumbling is considered complete when all of the angular velocities have absolute values less than 2×10^{-3}. The external disturbance is set as $\boldsymbol{d}(t) = 10^{-4} \times [1 + \sin(\frac{\pi t}{125}) + 1.5\sin(\frac{\pi t}{200}), 2 + 1.5\sin(\frac{\pi t}{125}) - 2\sin(\frac{\pi t}{200}), -1 + 2\sin(\frac{\pi t}{125}) - 1.5\sin(\frac{\pi t}{200})]^{\mathrm{T}}$ Nm. By the proposed controller in (43) with parameters $k_2 = 0.4$, $k_3 = 0.01$, $k_4 = 27$ and $\beta_\omega = 0.5$ satisfying the parameter condition of Theorem 2. To show the advantages of the proposed control scheme, the traditional P-controller $\boldsymbol{u} = -k_2\boldsymbol{\omega}$ with pseudo-inverse-based control allocation is used in the spacecraft de-tumbling control. The results are shown in Figures 6–8. Figure 6 shows the closed-loop system performance under P-controller with pseudo-inverse-based control allocation; Figure 7 shows the closed-loop system performance under proposed controller with pseudo-inverse-based control allocation; Figure 8 shows the closed-loop system performance under proposed controller with RobDCA.

It is observed from Figure 7 that the desired states can still be tracked with small tracking errors and a rapid convergence rate when the proposed scheme is used. Whereas for performance of the PD controller with a pseudo-inverse-based control allocation method in Figure 6, due to the inertia uncertainty and external disturbances, the steady-state of angular velocity is about 4×10^{-3} rad/s, which is much larger than that under the proposed scheme and also not satisfy the de-tumbling condition 2×10^{-3} rad/s. This is due to the fact that the proposed scheme contains the nonlinear disturbance observer (44) which possesses strong robustness

with respect to the considered form of inertia uncertainty and external disturbances. In Figure 8, the proposed RobDCA is also considered in the closed-loop. We can see that the convergence time is 800 seconds and the steady-state of angular velocity is less than 5×10^{-6}, where both the convergence time and magnitude of the steady-state of angular velocity is shorter than the same controller law with pseudo-inverse-based control allocation method. Moreover, the dynamics and uncertainty in the actuators are not considered in the pseudo-inverse method. The virtual control signals and thruster forces are shown in Figures 6–8 (b) and (c), respectively, in which the saturation effect is clearly seen. During 1500 seconds, it can be seen that the PD control requires an accumulated torque of 13.299 (Nm) and an accumulated force of 62.3818 N to perform the maneuver. The proposed controller with pseudo-inverse-based control allocation needs an accumulated torque of 13.6921 (Nm) and an accumulated force of 62.3818 N to perform the maneuver. The proposed controller with RobDCA needs an accumulated torque of 15.5539 (Nm) and an accumulated force of 98.3852 N to perform the maneuver. Comparing with the other two control schemes, the proposed controller with RobDCA method sees a small increase in the accumulated torque requirement, but with a significantly improved tracking performance.

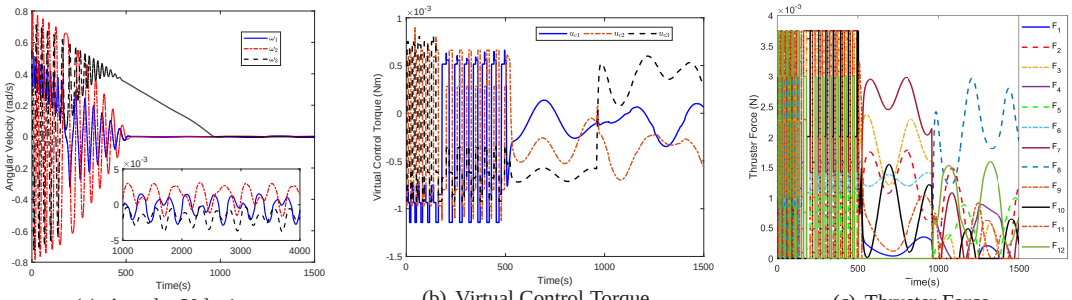

(a) Angular Velocity (b) Virtual Control Torque (c) Thruster Force

Figure 6: System performance under PD controller with pseudo-inverse-based control allocation

5.2. *Large angle slew manoeuver of combined spacecraft*

We assume the initial attitude MRPs of the combined spacecraft is $\boldsymbol{\sigma}(0) = [-0.206, -0.179, 0.075]^{\mathrm{T}}$, the initial angular velocity of the combined spacecraft is set to be zero. The controller parameters are set as $k_1 = 0.15$, $k_2 = 0.5$, $k_3 = 1$, $k_4 = 0.5$, $\beta = 27$ and $\tau = 1$, such that $2k_4k_2 > 3k_3^2k_5^2$, $2\beta k_2 > 3$, $16k_1 > 3r_M^2\tau$ with $k_5^2 = 4.5 \times 10^{-12}$ satisfying the parameter condition of Theorem 1. And the parameters of prescribed performance are presented in Table 4. To show the advantages of the proposed control scheme, the traditional *PD*-controller $\boldsymbol{u} = -k_\sigma\boldsymbol{\sigma} - k_\omega\boldsymbol{\omega}$ [44] with pseudo-inverse-based control allocation is used in the

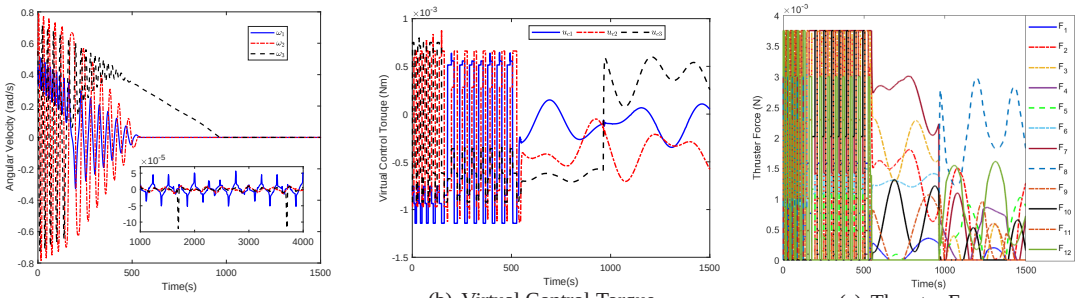

(a) Angular Velocity (b) Virtual Control Torque (c) Thruster Force

Figure 7: System performance under proposed controller with pseudo-inverse-based control allocation

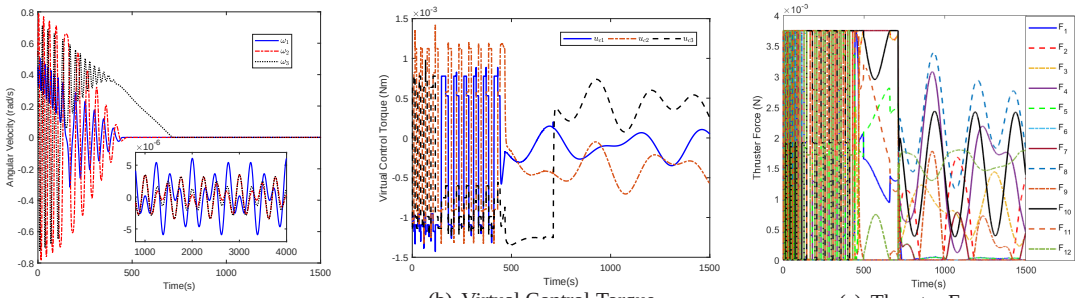

(a) Angular Velocity (b) Virtual Control Torque (c) Thruster Force

Figure 8: System performance under proposed controller with RobDCA

spacecraft slew manoeuver control. The simulation results are shown in Figures 9–14. Figures 9–11 present the time history of attitude trajectories by the traditional *PD*-controller and proposed DSC+PPC method with pseudo-inverse-based control allocation, and proposed DSC+PPC method with RobDCA, respectively. Figures 12–14 present the other closed-loop system performance under *PD*-controller (PD+PI) and proposed control method (PPC+PI) with pseudo-inverse-based control allocation, and proposed control method with RobDCA (PPC+RobDCA), respectively. In the Figures 9–11, PPB means prescribed-performance bound.

Table 4 Performance function parameters

i-th	ρ_{i0}	$\rho_{i\infty}$	γ_i	$\eta_{i\,\min}$	$\eta_{i\,\max}$
1	0.25	3×10^{-5}	0.025	1	0.1
2	0.28	1.4×10^{-5}	0.03	1	0.1
3	0.095	5×10^{-5}	0.02	0.2	1

As we can see from Figures 9–11, by the method of PPC+RobDCA, the attitude can also converge to zero within prescribed-performance bounds, while PD+PI and PPC+PI can not ensure this performance. In Figures 12–14, the magnitude of the angular velocity based on PPC+RobDCA is smaller than 6×10^{-6} rad/s after 200 seconds, while PPC+PI can only ensure the magnitude of the angular velocity within 1×10^{-4} better than PD+PI after 200 seconds. Also, as we can see from Figures 12–14 (b) and (c), the trajectories of all the virtual control torques and thruster forces are approximately the same. The trajectories of virtual control using the proposed DSC+PPC method is smoother than the others considered here.

5.3. Necessity to rebuild the new attitude dynamics

In this subsection, we illustrate the necessity to rebuild the new attitude dynamics of the combined system rather than using the original equations expressed in the chaser frame. In the case that the original equations expressed in the chaser frame are used the inclusion of the target dynamics is simply added as a disturbance. However, the target spacecraft has the same size as the chaser spacecraft, so this uncertain disturbance is considerably large and must be compensated for by the controller. Here we use the proposed control of this paper to both models to demonstrate the need to re-construct the dynamic equations of motion of the combined system. Since the thrusters' configuration matrix of the chaser spacecraft has been determined and there is no uncertainty in the configuration matrix, pseudo-inverse-based control allocation method will used. With the same proposed method, we have the results shown in Figures 15–17. Figure 15 shows the closed-loop system performance of the target spacecraft by proposed controller when de-tumbling the combined spacecraft CubSat. The time history of attitude trajectories are shown in Figures 16–17. Due to

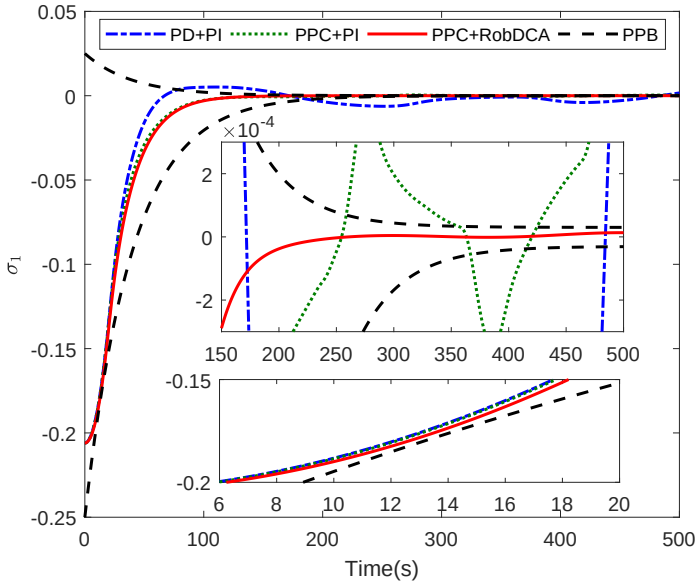

Figure 9: Time histories of spacecraft attitude with three control scheme

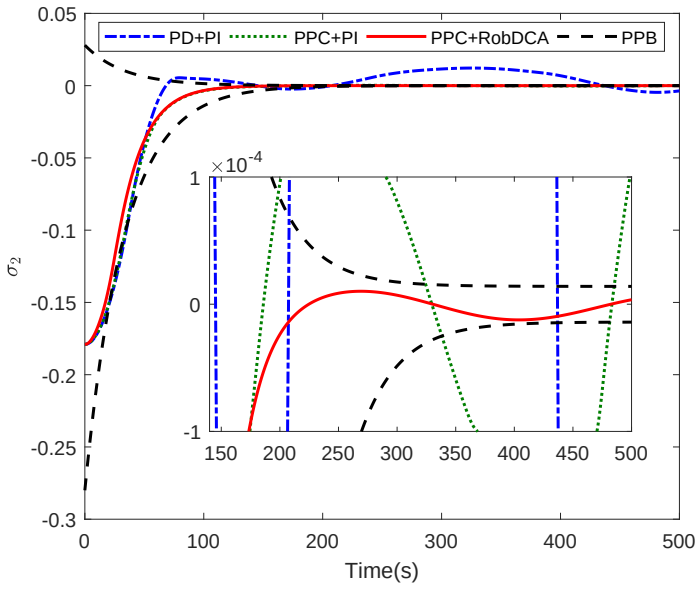

Figure 10: Time histories of spacecraft attitude with three control scheme

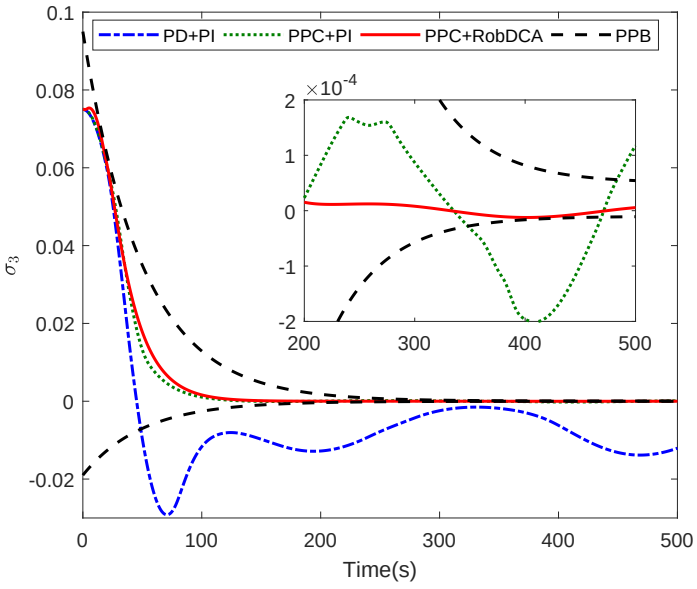

Figure 11: Time histories of spacecraft attitude with three control scheme

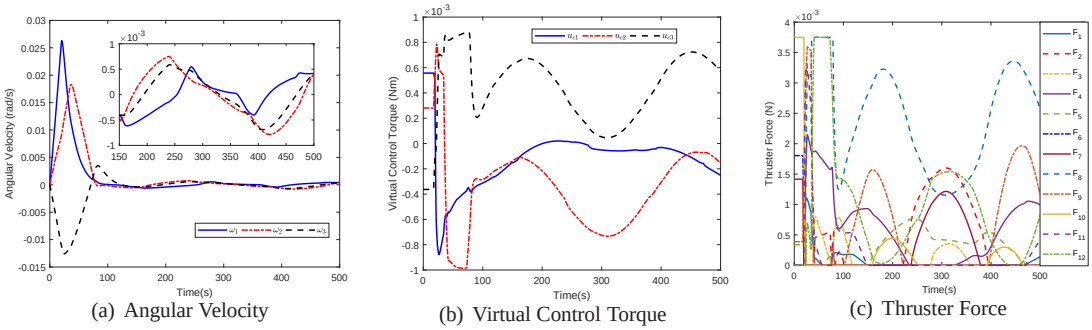

(a) Angular Velocity (b) Virtual Control Torque (c) Thruster Force

Figure 12: System performance under PD controller with pseudo-inverse-based control allocation

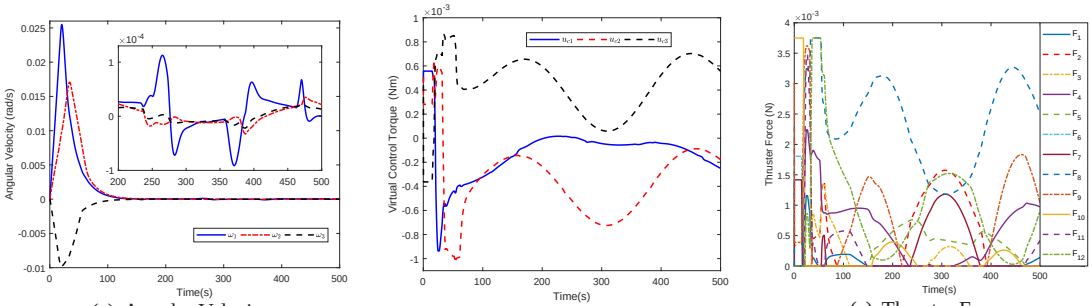

(a) Angular Velocity (b) Virtual Control Torque (c) Thruster Force

Figure 13: System performance under proposed controller with pseudo-inverse-based control allocation

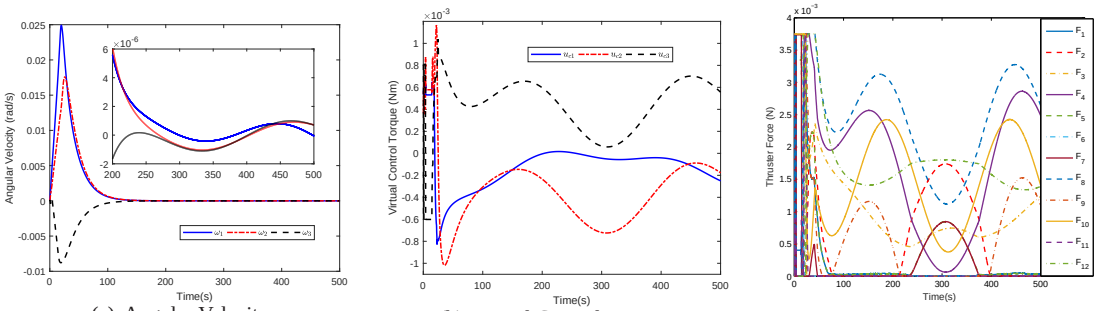

(a) Angular Velocity (b) Virtual Control Torque (c) Thruster Force

Figure 14: System performance under proposed controller with RobDCA

large inertia uncertainty, it is observed from Figure 15 that the magnitude of the angular velocity exceeds 5×10^{-3} rad/s during some period, which does not satisfy the de-tumbling condition. As we can see from Figure 16, based on the attitude dynamics of the target spacecraft, the magnitude of the attitude exceeds 0.03 at nearly 1000 seconds. In Figure 17, the same result comes also in the attitude velocity, the magnitude of the angular velocity exceeds 4×10^{-3} rad/s at nearly 1000 seconds. The simulations demonstrate that if the dynamics of the combined spacecraft are not re-constructed in-situ then the control performance can be poor. Moreover, the control implemented based on the combined dynamic model sees significant improvement in performance.

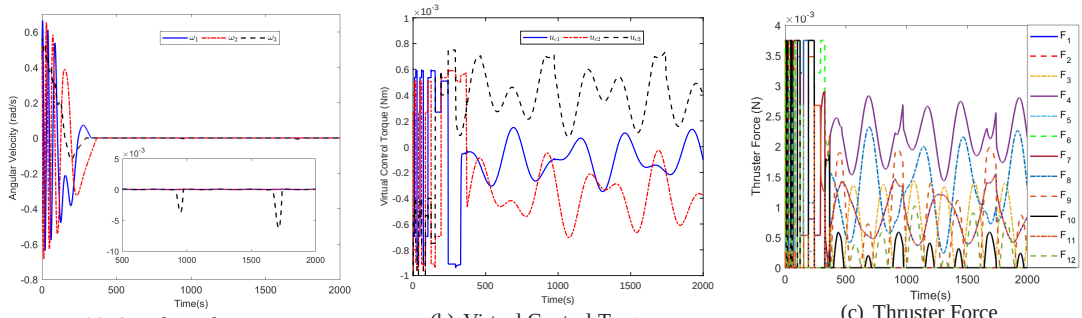

(a) Angular Velocity (b) Virtual Control Torque (c) Thruster Force

Figure 15: System performance under proposed controller with normal attitude dynamics

6. Conclusion

In this paper, a dynamic surface method incorporating a robust dynamic control allocation strategy has been proposed for attitude control of a combined chaser-target system. The results demonstrate the importance of reconstructing the dynamic model of the combined system in a reference frame at the new centre-of-mass. Moreover, developing a robust control based on a large disturbance to the chaser dynamics, rather than re-building the dynamic model in-situ, yields poor performance. A disturbance-observer-based dynamic surface method is developed, which is robust to external disturbances as well as any modelling errors in the re-constructed dynamics. Furthermore, this control allows the performances to be prescribed a priori and avoids the "explosion of complexity" associated with the backstepping method.

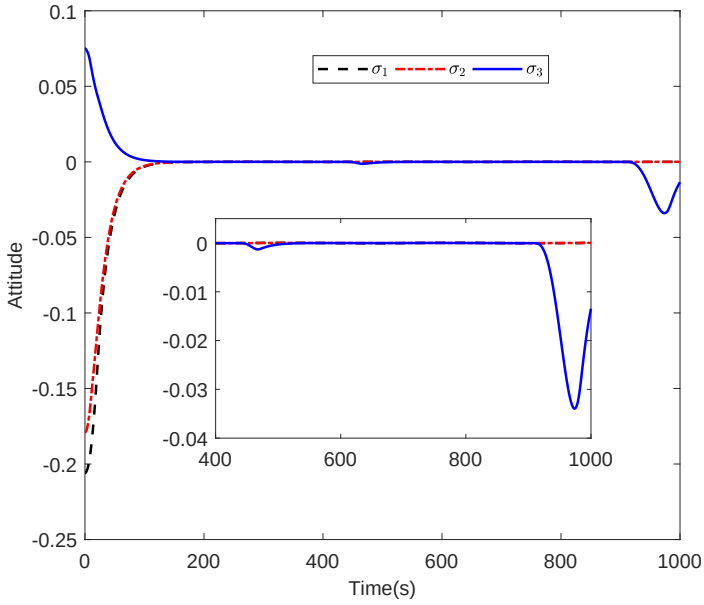

Figure 16: Time histories of spacecraft attitude with normal attitude dynamics

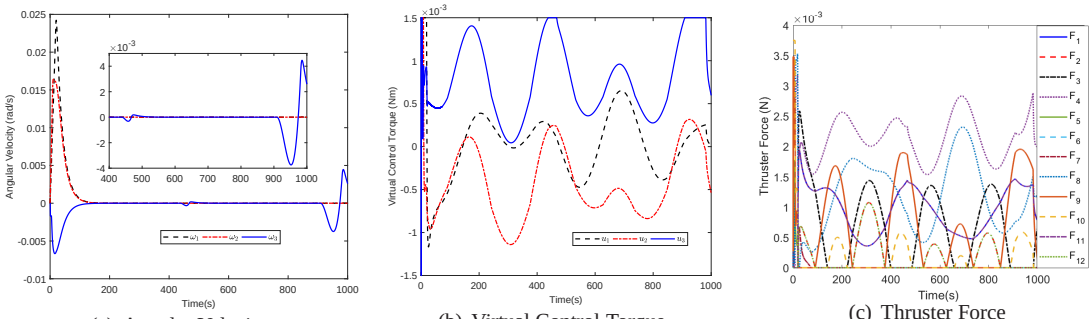

(a) Angular Velocity (b) Virtual Control Torque (c) Thruster Force

Figure 17: System performance under proposed controller with normal attitude dynamics

7. Acknowledgments

This work is supported by the Major Program of National Natural Science Foundation of China (Nos. 61690210, 61690212), Self-Planned Task (No. SKLRS201716A) of State Key Laboratory of Robotics and System (HIT) and the National Natural Science Foundation of China (No. 61333003).

References

[1] Q. Li, J. Yuan, B. Zhang, C. Gao, Model predictive control for autonomous rendezvous and docking with a tumbling target, Aerosp. Sci. Technol. 69 (2017) 700–711.

[2] Y. Sun, Y. Deng, H. Duan, X. Xu, Bionic visual close-range navigation control system for the docking stage of probe-and-drogue autonomous aerial refueling, Aerosp. Sci. Technol. 91 (2019) 136–149.

[3] J. Virgili-Llop, J. V. Drew, R. Zappulla, M. Romano, Laboratory experiments of resident space object capture by a spacecraftmanipulator system, Aerosp. Sci. Technol. 71 (2017) 530–545.

[4] Y. Wu, F. Han, M. Zheng, F. Wang, B. Hua, Z. Chen, Y. Cheng, Attitude tracking control for a space moving target with high dynamic performance using hybrid actuator, Aerosp. Sci. Technol. 78 (2018) 102–117.

[5] T. Nguyen-Huynh, I. Sharf, Adaptive reactionless motion and parameter identification in postcapture of space debris, J. Guid. Control Dyn. 36 (2) (2013) 404–414.

[6] H. Gao, G. Ma, Y. Lv, Y. Guo, Forecasting-based data-driven model-free adaptive sliding mode attitude control of combined spacecraft, Aerosp. Sci. Technol. 86 (2019) 364–374.

[7] J. Slotine, M. Benedetto, Hamiltonian adaptive control of spacecraft, IEEE Trans. Automat. Contr. 35 (7) (1990) 848–852.

[8] G. Falcone, A. Saxena, S. Bandyopadhyay, S. J. Chung, F. Hadaegh, Attitude control of the asteroid redirect robotic mission spacecraft with a captured boulder, AIAA/AAS Astrodynamics Specialist Conference 35 (7) (1990) 848–852.

[9] R. W. A Sofyalı, E M Jafarov, Robust and global attitude stabilization of magnetically actuated spacecraft through sliding mode, Aerosp. Sci. Technol. 76 (2018) 91–104.

[10] F. Zhang, G. Duan, Robust adaptive integrated translation and rotation control of a rigid spacecraft with control saturation and actuator misalignment, Acta Astronaut. 86 (2013) 167–187.

[11] P. Huang, M. Wang, Z. Meng, F. Zhang, Z. Liu, H. Chang, Reconfigurable spacecraft attitude takeover control in post-capture of target by space manipulators, J. Franklin Inst. 353 (9) (2016) 1985–2008.

[12] Q. Hu, G. Niu, C. Wang, Spacecraft attitude fault-tolerant control based on iterative learning observer and control allocation, Aerosp. Sci. Technol. 75 (2018) 254–253.

[13] J. Luo, C. Wei, H. Dai, Z. Yin, X. Wei, J. Yuan, Robust inertia-free attitude takeover control of post-capture combined spacecraft with guaranteed prescribed performance, ISA Trans. 74 (2018) 28–44.

[14] O. Haerkegard, Dynamic control allocation using constrained quadratic programming, J. Guid. Control Dyn. 27 (6) (2004) 1028–1034.

[15] A. Zhang, Q. Hu, X. Huo, Dynamic control allocation for spacecraft attitude stabilization with actuator uncertainty, P. I. Mech. Eng. C-J Mec. 228 (8) (2013) 1336–1347.

[16] C. Guo, X. Liang, Integrated guidance and control based on block backstepping sliding mode and dynamic control allocation, P. I. Mech. Eng. C-J Mec. 229 (9) (2014) 1559–1574.

[17] S. Almutairi, N. Aouf, Reconfigurable dynamic control allocation for aircraft with actuator failures, Aeronaut. J. 121 (1237) (2017) 341–371.

[18] C. Bechlioulis, G. Rovithakis, Robust adaptive control of feedback linearizable mimo nonlinear systems with prescribed performance, IEEE Trans. Automat. Contr. 53 (9) (2008) 2090–2099.

[19] C. Bechlioulis, G. Rovithakis, Adaptive control with guaranteed transient and steady state tracking error bounds for strict feedback systems, Automatica 45 (2) (2009) 532–538.

[20] C. Ming, R. Sun, B. Zhu, Nonlinear fault-tolerant control with prescribed performance for air-breathing supersonic missiles, J. Spacecraf Rockets 54 (5) (2017) 1092–1099.

[21] Q. Hu, X. Shao, L. Guo, Adaptive fault-tolerant attitude tracking control of spacecraft with prescribed performance, IEEE/ASME Trans. Mech. 23 (1) (2018) 331–341.

[22] Y. Bai, J. Biggs, F. Zazzera, N. Cui, Adaptive attitude tracking with active uncertainty rejection, J. Guid. Control Dyn. 41 (1) (2017) 550–558.

[23] Y. Bai, J. D. Biggs, X. Wang, N. Cui, A singular adaptive attitude control with active disturbance rejection, Eur. J. Control 35 (2017) 50–56.

[24] L. Guo, W. Chen, Disturbance attenuation and rejection for systems with nonlinearity via dobc approach, Int. J. Robust Nonlin. 15 (3) (2005) 109–125.

[25] S. Han, J. Lee, Fuzzy echo state neural networks and funnel dynamic surface control for prescribed performance of a nonlinear dynamic system, IEEE Trans. Ind. Electron. 61 (2) (2014) 1099–1112.

[26] S. Li, Z. Xiang, Adaptive prescribed performance control for switched nonlinear systems with input saturation, Int. J. Syst. Sci. 49 (1) (2017) 113–123.

[27] C. Wang, G. Yang, Observer-based adaptive prescribed performance tracking control for nonlinear systems with unknown control direction and input saturation, Neurocomputing 284 (2018) 17–26.

[28] Z. Peng, J. Wang, J. Wang, Constrained control of autonomous underwater vehicles based on command optimization and disturbance estimation, IEEE T Ind Electron 66 (2019) 3627–3635.

[29] L. Sun, Z. Zheng, Disturbance-observer-based robust backstepping attitude stabilization of spacecraft under input saturation and measurement and uncertainty, IEEE Trans. Ind. Electron. 64 (10) (2017) 7994–8002.

[30] B. Xu, C. Yang, Y. Pan, Global neural dynamic surface tracking control of strict-feedback systems with application to hypersonic flight vehicle, IEEE Trans. Neur. Net. Lear. 26 (10) (2015) 2563–2575.

[31] C. Wang, Y. Lin, Adaptive dynamic surface control for mimo nonlinear time-varying systems with prescribed tracking performance, Int. J. Control 88 (4) (2015) 832–843.

[32] P. Huang, M. Wang, Z. Meng, F. Zhang, Z. Liu, Attitude takeover control for post-capture of target spacecraft using space robot, Aerosp. Sci. Technol. 51 (2016) 171–180.

[33] A. Flores-Abad, O. Ma, K. Pham, S. Ulrich, A review of space robotics technologies for on-orbit servicing, Prog. Aerosp. Sci. 68 (2014) 1–26.

[34] O. Ma, H. Dang, K. Pham, On-orbit identification of inertia properties of spacecraft using a robotic arm, J. Guid. Control Dyn. 31 (6) (2008) 1761–1771.

[35] B. Huo, Y. Xia, L. Yin, M. Fu, Fuzzy adaptive fault-tolerant output feedback attitude -tracking control of rigid spacecraft, IEEE Trans. Syst. Man CY-S 47 (8) (2017) 1898–1908.

[36] R. Pena, R. Alonso, P. Anigstein, Robust optimal solution to the attitude/force control problem, IEEE Trans. Aero. Elec. Sys. 36 (3) (2000) 784–792.

[37] C. Song, S. Kim, S. Kim, H. Nam, Robust control of the missile attitude based on quaternion feedback, Control Eng. Pract. 14 (7) (2006) 811–818.

[38] M. Chen, B. Ren, Q. Wu, C. Jiang, Anti-disturbance control of hypersonic flight vehicles with input saturation using disturbance observer, Sci. China Inform. Sci. 58 (7) (2015) 1–12.

[39] C. Benchlioulis, G. Rovithakis, A low-complexity global approximation free control scheme with prescribed performance for unknown pure feedback systems, Automatica 50 (4) (2014) 1217–1226.

[40] D. Zhou, B. Xu, Adaptive dynamic surface guidance law with input saturation constraint and autopilot dynamics, J. Guid. Control Dyn. 39 (5) (2016) 1155–1162.

[41] Q. Shen, D. Wang, S. Zhu, E. Poh, Postcapture robust nonlinear control for tethered space robot with constraints on actuator and velocity of space tether, IEEE Trans. Contr. Syst. T. 25 (3) (2017) 1068–1075.

[42] G. Duan, H. Yu, Lmis in control systems: analysis, design and applications, CRC press, 2013.

[43] H. Henninger, J. Biggs, Near time-minimal earth to l_1 transfers for low-thrust spacecraft, J. Guid. Control Dyn. 40 (11) (2017) 2999–3004.

[44] J. Wen, K. Kreutz-Delgado, The attitude control problem, IEEE Trans. Automat. Contr. 36 (10) (1991) 1148–1162.